Journal of Energy Chemistry 75 (2022) 457–477

Contents lists available at ScienceDirect

Journal of Energy Chemistry

journal homepage: www.elsevier.com/locate/jechem

http://www.journals.elsevier.com/journal-of-energy-chemistry/

Review

Assembly and electrochemical testing of renewable carbon-based anodes in SIBs: A practical guide

Darío Alvira *, Daniel Antorán, Joan J. Manyà

Aragón Institute of Engineering Research (I3A), Thermochemical Processes Group, University of Zaragoza, Escuela Politécnica Superior, 22071 Huesca, Spain

ARTICLE INFO

Article history:
Received 19 April 2022
Revised 25 August 2022
Accepted 2 September 2022
Available online 9 September 2022

Keywords:
Sodium-ion battery
Anode
Hard carbon
Electrochemical techniques
Carbon characterization

ABSTRACT

Sodium-ion batteries (SIBs) are considered as a promising candidate to replace lithium-ion batteries (LIBs) in large-scale energy storage applications. Abundant sodium resources and similar working principles make this technology attractive to be implemented in the near future. However, the development of high-performance carbon anodes is a focal point to the upcoming success of SIBs in terms of power density, cycling stability, and lifespan. Fundamental knowledge in electrochemical and physicochemical techniques is required to properly evaluate the anode performance and move it in the right direction. This review aims at providing a comprehensive guideline to help researchers from different backgrounds (e.g., nanomaterials and thermochemistry) to delve into this topic. The main components, lab configurations, procedures, and working principles of SIBs are summarized. Moreover, a detailed description of the most used electrochemical and physicochemical techniques to characterize electrochemically active materials is provided.

© 2022 Science Press and Dalian Institute of Chemical Physics, Chinese Academy of Sciences. Published by ELSEVIER B.V. and Science Press. This is an open access article under the CC BY-NC-ND license (http://creativecommons.org/licenses/by-nc-nd/4.0/).

Contents

1. Introduction . . . 458
2. Working principle and components of SIBs . . . 458
   2.1. Current collectors . . . 459
   2.2. Insulator . . . 459
   2.3. Separator . . . 459
   2.4. Counter electrode . . . 459
   2.5. Working electrode . . . 460
      Binder compounds . . . 461
   2.6. Reference electrode . . . 462
   2.7. Electrolyte . . . 463
      2.7.1. Alkyl carbonate-based electrolytes . . . 463
      2.7.2. Electrolyte additives . . . 463
      2.7.3. Other electrolytes . . . 464
3. Carbonaceous electrode preparation for lab scales . . . 464
4. Types of cells . . . 465
5. Electrochemical techniques . . . 466
   5.1. Fundamental electrochemical concepts . . . 466
   5.2. Potentiodynamic techniques . . . 467
   5.3. Galvanodynamic techniques . . . 468
   5.4. Impedance-based techniques . . . 469
   5.5. Two vs. three electrode setup . . . 470
      5.5.1. Undervalued rate capability . . . 470

* Corresponding author.
E-mail address: dalvira@unizar.es (D. Alvira).

https://doi.org/10.1016/j.jechem.2022.09.002
2095-4956/© 2022 Science Press and Dalian Institute of Chemical Physics, Chinese Academy of Sciences. Published by ELSEVIER B.V. and Science Press.
This is an open access article under the CC BY-NC-ND license (http://creativecommons.org/licenses/by-nc-nd/4.0/).

5.5.2. EIS misinterpretations . . . 471
6. Carbon characterization techniques . . . 472
7. Conclusions and prospects. . . . 473
Declaration of competing interest . . . 473
Acknowledgments . . . 473
References . . . 473

1. Introduction

The growth of green energies from intermittent renewable sources and the prospective electric vehicle expansion entails the employment of sustainable and low-cost energy storage systems (ESSs). Since the 1990s, lithium-ion batteries (LIBs) are the widely used rechargeable batteries due to their high reversible capacity and cycling stability. Nevertheless, the increasing demand for lithium and other LIBs basic components with limited or geographically concentrated reserves (e.g., cobalt and natural graphite) [1], forces us to explore new, cheaper, and based on more earth abundant elements ESSs.

Sodium-ion batteries (SIBs) are a reasonable alternative to replace LIBs since sodium and lithium are neighbors in the alkali metals group, showing similar physical and chemical properties. Both have comparable standard electrode potentials (−3.04 V vs. SHE for Li/Li^+ and −2.71 V vs. SHE for Na/Na^+) and both easily form cations Li^+ and Na^+ from a loosely bound electron in their outer shell. Moreover, sodium is cheaper, considerably more abundant than lithium in the earth's crust (2.36 wt% vs. 0.0017 wt%) and widely dispersed around the continents [2,3]. In addition, sodium-ion batteries offer other advantages, such as the following:

i. Carbon-based anodes, instead of graphite-based ones, have the potential to improve battery's performance by easily modifying their structural, chemical, and electrochemical characteristics.
ii. In contrast with lithium-ion batteries, aluminum can be used as a current collector for both electrodes since it doesn't form any alloy with sodium, reducing weight and cost versus the copper current collector used in LIB anodes [4].
iii. Both aluminum current collectors allow SIBs to be discharged and stored at 0 V without degradation or safety risks. This is not possible in LIBs due to Al/Li alloying reactions at a voltage window comprised between −0.1 and 1 V and because dissolution of Cu from the negative current collector leads to a decrease in the discharge capacity and cyclic life [5,6].
iv. The desolvation energy for Na ions in several organic solvents is about 30% smaller than that for Li ions. As a result, charge transfer resistance at the electrode–electrolyte interface is smaller, providing better electrode kinetics [7,8].
v. Layered lithium transition-metal oxides Li_xTMO_2 ($x \leq 1$, TM = transition-metal) are the main commercial cathode material for current LIBs. Whereas Ni and Co are used in LIBs, almost all first-row transition-metal elements can be used in SIBs. This is due to the higher size difference between the Na-ion (0.102 nm) and the transition-metal ions (0.05–0.07 nm), which facilitates its separation [9].
vi. Same conductive carbon filler, binder materials and aprotic electrolyte solvents used in LIBs can also be employed in SIBs. Moreover, similar technology, working principles and equipment allow to use same industrial processes and, therefore, to facilitate the adaptation of current manufacturing processes for SIBs purposes [10].

Nevertheless, SIBs know-how is still in an early development stage and there is a long way to go until achieving the full potential of this technology. In this respect, the design of high-performance anodes is one of the main challenges, since in contrast to LIBs, Na ions cannot be intercalated into a graphite electrode. Anodes based on carbonaceous materials, especially hard carbons (HCs), are the main candidates to be assembled in commercial SIBs. Nevertheless, the Na^+ storage mechanism is still in discussion and a better understanding is required to design engineered carbons with better performances.

To reach the necessary in-depth knowledge about the carbon optimal characteristics, an interdisciplinary approach from the thermochemistry, electrochemistry, and materials field is required. We think that it can be hindered by the absence of clear and practical guidelines on the assembly and characterization of batteries, especially for those not coming from the electrochemical field. This review aims at providing an overview of the available setups and characterization techniques for SIBs, which can be helpful for researchers from different backgrounds. As a starting point, the main components and working principles of SIBs are summarized, with special emphasis on the carbonaceous electrode preparation (e.g., binders and manufacturing). Next, different cell types and configuration for lab-scale devices are presented. Finally, a detailed description of the most used electrochemical and physicochemical characterization techniques is provided.

2. Working principle and components of SIBs

Analogous to lithium-ion batteries, each sodium-ion cell is made up of a positive and a negative electrode, a separator surrounded by an electrolyte, and two current collectors. Inside this closed system, for every electron generated in an electrode oxidation, other electron is consumed in the reduction reaction occurred on the opposite electrode. The electrochemical function of both electrodes switches between the anode (oxidation) and cathode (reduction) in accordance with the current direction. In the field of batteries, however, the positive and negative electrodes are usually designed as the cathode and anode, respectively (see Fig. 1). During battery charging (orange arrows), electrons from the cathode oxidation move through the external circuit towards the negative electrode. Concurrently, in order to preserve charge neutrality, Na ions pass through the electrolyte and separator to be hosted in the anode. The opposite process occurs during the battery discharging (blue arrows), supplying electric power to external devices.

The formation of passivation films during the first charge cycles also determines the cell behavior. The electrolyte reduction on the anode surface results in the solid electrolyte interphase (SEI) while the electrolyte oxidation on the cathode creates the solid permeable interface (SPI). These passivation layers protect the electrodes along cycles, blocking the electron transport as pure cationic conductors and avoiding further electrolyte degradation [11,12]. Nevertheless, an excessive growth of the SEI gives rise to sodium ion trapping and the subsequent capacity loss and energy density drop. An additional issue to consider is the possible formation of dendrites on the negative electrode during the charge. Dendrites are

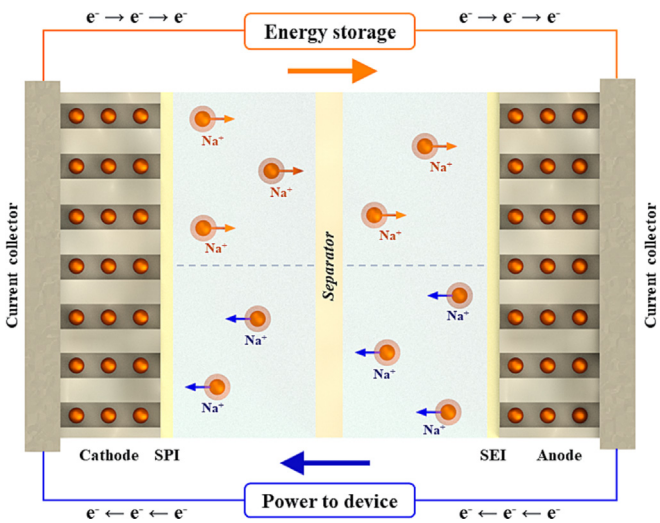

Fig. 1. Working principle of sodium ion batteries.

metallic microstructures formed by electrochemical deposition of sodium that, in case of a rapid increase in height, may penetrate the separator causing internal short circuiting [13]. In the following sections, the description of the different components of a SIB is provided, with a special emphasis on the different materials studied to date for each part of de device.

2.1. Current collectors

Current collectors need to be good electron conductors and are designed to transfer electrons from the external circuit to the active materials of the cell [13]. The choice of the current collector is relevant since reactions on its surface can limit the operating potential window of the cell. The current collector placed at the cathode side can suffer corrosion depending on the electrolyte salt composition. Stainless steel foils can be used, although aluminum is the preferred material. A thin passive film developed on the metal surface makes aluminum more stable at high anodic potentials and allows the maximum cell voltage to increase [14].

At the anode side, the voltage window can be altered if the current collector reacts with the cation to form alloys. In lithium-ion batteries, cooper and aluminum foils are commonly used as current collectors for the anode and cathode, respectively. Using Cu instead of cheaper Al is due to the electrochemical formation of an amorphous Li-Al alloy at around 0.3 V vs. Li/Li^+ [15,16]. However, since aluminum does not form an alloy with sodium, it can be used as an anode current collector in SIBs [17]. In addition to being a cheaper choice, aluminum also shows better overall stability than copper, as well as AISI 304 and AISI 316 stainless steels [18]. Because sodium can be alloyed with tin and lead, special care must be taken regarding the aluminum purity grade [19].

2.2. Insulator

Depending on the cell type (see Section 4), an insulator is required to avoid contact between current collectors and to prevent the cell from short-circuit. Biaxially-oriented polyethylene terephthalate (BoPET), also known by the brand names Mylar, Melinex or Hostaphan, is a popular insulator for LIBs. However, it undergoes degradation processes in contact with some electrolyte decomposition products to form highly reactive radical species [20]. Meanwhile, polyamides (PA) as Nylon, despite being widely used in Ni-Cd and Ni-MH batteries, do not seem to be appropriate for SIBs due to its degradation in alkaline media [21].

Polytetrafluoroethylene (PTFE), also known as Teflon, is commonly used to cover battery plungers. Nevertheless, in contact with alkali metals at low voltages (below 5 V) it gets defluorinated and forms carbon. The reduction of PTFE can affect the coulombic efficiency of the cell and might even cause an internal short circuit since the produced carbon can be conductive [22–24]. In the case of sodium, PTFE decomposition was observed in diglyme-based solvents [25]; however, no evidence was found when carbonates-based solvents were used [26]. By contrast, polyether ether ketone (PEEK) is resistant to highly alkaline media [27] and has been used in SIBs without problems [28]. Finally, polyolefins (PO) such as polypropylene and high-density polyethylene present higher stability than PTFE at low potentials [29]. Because of their low reactivity, polyolefins are used as insulators [30] and even as separators [31] in cells. In conclusion, PEEK and polyolefins seem to be the best materials to be chosen as insulators for SIBs.

2.3. Separator

Separators or diaphragms are used to separate the electrolyte solution surrounding the working electrode from the electrolyte solutions adjacent to the counter and reference electrodes. This electronic insulation has to prevent physical contact between electrodes, but ensuring ionic transportation through its micro-sized pores [13,29]. Polyolefin and glass fiber membranes are the two widely employed separator types in lab-scale setups [26].

Polyolefin membranes, mostly provided by Celgard™, are composed of polypropylene and polyethylene. These separators are the dominant ones in commercial LIBs because of their thinness (<30 μm), mechanical strength, pore structure, electrochemical stability, and thermal shutdown properties [29]. However, in lab-scale setups —where the thickness is not an impediment— the use of glass fiber membranes (borosilicate glass) is preferred, since they provide excellent chemical stability [26], higher liquid electrolyte uptake [32], and better thermal stability [33]. Laboratory fiberglass filters can be used for this purpose. Furthermore, it should be pointed out that other advanced materials are being studied as separators in SIBs; for instance, barium titanate-based porous ceramic flexible membranes [34] and composites derived from cellulose [35].

2.4. Counter electrode

A counter or auxiliary electrode is the one whose purpose is to compensate (according to the passed charge and without significant parasitic reactions) for the processes taking place at the working electrode [13]. Since this review is focused on the study of carbonaceous anodes, the cathode or positive electrode will be treated as the counter electrode. A suitable counter electrode (CE) must enable the reversible store charging of the working electrode (WE). Thus, it should offer fast reaction kinetics and highly enough capacity to enable the complete WE sodiation. Moreover, reactions occurring in the counter electrode should neither affect nor contaminate the cell system.

For a certain ion battery, the corresponding alkali metal (metallic sodium for SIBs) has the highest theoretical capacity as counter electrode [26]. Nonetheless, no alkali metal electrodes are used in commercial LIBs or SIBs due to safety risks arising from the high reactivity of the metal as well as the probable growth of dendrites. Regarding the development of cathode materials for SIBs, sodium transition metal oxides (TMOs) with a Na_xMO_2 type structure (M = transition metal) are the most studied so far (see Table 1). Some examples are $NaCrO_2$ [36,37], Na_xCoO_2 [38–40], $Na_xMn_yO_2$ [41–43], $Na_xFe_yMn_yO_2$ [44,45], $Na_xNi_yMn_zCO_tO_2$ [46,47], $Na_xNi_yMn_yO_2$ [48,49], and $Na_xNi_yFe_zMn_yO_2$ [50–52]. Polyanionic compounds are also potential candidates, including olivine-type

Table 1
Performance of several cathode materials.

Cathode material	Voltage range (V)	Specific capacity (mAh g^{-1})	Rate capability (mAh g^{-1})	Capacity retention	Ref.
Sodium transition metal oxides (TMOs)					
$NaCrO_2$	2.0–3.6	120 (240 mA g^{-1})	76.7 (4.8 A g^{-1})	80.86% (900 cycles)	[71]
$Na_{0.7}CoO_2$	2–3.8	112 (50 mA g^{-1})	84 (1 A g^{-1})	86% (300 cycles)	[72]
$Na_{0.44}MnO$	1.5–4	120 (50 mA g^{-1})	69.5 (1.2 A g^{-1})	93% (150 cycles)	[73]
$Na_{2/3}Fe_{1/2}Mn_{1/2}O_2$	1.5–4	126.3 (13 mA g^{-1})	97.8 (0.260 A g^{-1})	75.6% (30 cycles)	[74]
$Na_{0.55}Ni_{0.1}Fe_{0.1}Mn_{0.8}O_2$	1.5–4.3	221.5 (12 mA g^{-1})	85 (2.4 A g^{-1})	75% (100 cycles)	[75]
Polyanionic compounds					
$NaFePO_4$	2–4	140 (15 mA g^{-1})	60 (1.15 A g^{-1})	92% (200 cycles)	[76]
$Na_3V_2(PO_4)_3$	2–3.9	115 (23.4 mA g^{-1})	104 (2.3 A g^{-1})	70% (10000 cycles)	[77]
$Na_{3.1}V_2(PO_4)_{2.9}(SiO_4)_{0.1}$	2.3–3.9	109.4 (22 mA g^{-1})	82.5 (2.2 A g^{-1})	98% (500 cycles)	[78]
$Na_3V_{1.9}(Ca,Mg,Al,Cr,Mn)_{0.1}(PO_4)_2F_3$	2–4.5	118.5 (12 mA g^{-1})	71.4 (6 A g^{-1})	90.2% (400 cycles)	[79]
PBAs					
$Na_{1.92}Fe_2(CN)_6$	2–4.25	157 (15 mA g^{-1})	145 (1.5 A g^{-1})	80% (750 cycles)	[80]
$Na_2Mn[Mn(CN)_6]$	1.2–4	209 (40 mA g^{-1})	157 (1 A g^{-1})	75% (100 cycles)	[81]
$Na_2CoFe(CN)_6$	2–4.1	153 (10 mA g^{-1})	60 (0.5 A g^{-1})	90% (200 cycles)	[82]
$Na_{0.7}Ti[Fe(CN)6]_{0.9}$	2–4.2	92.3 (50 mA g^{-1})	35.4 (0.4 A g^{-1})	70% (50 cycles)	[83]
Organic materials					
$Na_2C_6O_6$	0.5–3.2	498 (50 mA g^{-1})	371 (1 A g^{-1})	83.4% (50 cycles)	[68]
$Na_4C_8H_2O_6$	0.1–1.8	186 (18.7 mA g^{-1})	117 (0.935 A g^{-1})	89% (100 cycles)	[70]
Calix[4]quinone/Carbon	1.2–4.2	435 (0.1 C)	170 (1 C)	46% (100 cycles)	[84]

($NaFePO_4$) [53,54], NASICON-type ($Na_3V_2(PO_4)_3$) [55,56], sulfates ($Na_2M(SO_4)_2{\cdot}nH_2O$) [57], fluorophosphates (Na_xMPO_4F) [58–62], fluorosulfates ($NaMSO_4F$) [63], silicates (Na_2MSiO_4) [64], and pyrophosphates as $Na_7V_3(P_2O_7)_4$ [65]. Moreover, Prussian blue analogues (PBAs) have gained interest during the last years because of their low cost, open framework structure, and long cycle stability [66,67]. Finally, carbonyl-based organic salts such as $Na_2C_6O_6$ [68], $C_6Cl_4O_2$ [69], and $Na_4C_8H_2O_6$ [70] have recently been considered due to their sustainability and universal availability in natural systems.

When the electrode of interest (WE) is tested against sodium metal, the battery is called "half-cell", whereas when both cathode and anode are being analyzed simultaneously the battery is named "full cell" [85]. Half-cells are mainly used when the study is focused on the development of the anode. However, even though this simpler cathode is only used to provide charges to the working electrode, some aspects must be considered. A solid permeable interface (SPI) appears when the sodium metal electrode is in contact with the electrolyte. This electronically insulating and ion-conducting surface layer passivates the active metal and protects it from corrosion thanks to electron transfer blocking [86]. As studied for LIBs, the movement of the cation from the electrolyte to the CE requires desolvation at the SPI/electrolyte interface, mass transport through the SPI, and charge transfer at the SPI/metal interface [87,88]. The higher solubility of SPI compounds originated in SIBs may hinder the formation of a functional and stable solid electrolyte interphase [89,90], and special care must be taken with the electrochemical measurements made at the anode (see Section 5.5).

2.5. Working electrode

The working electrode is the electrode at which a given electrode process is examined [13] and, according to the topic of this review, it refers to the negative electrode (anode). Since graphite is not able to intercalate Na ions [91] and metallic sodium is not a suitable candidate due to the formation of dendrites [92] and high reactivity against electrolyte [89], alloy-, conversion-, organic-, and insertion-based electrodes are being studied for SIBs (see Fig. 2).

i) Alloying electrodes are based on the sodium alloying and dealloying reaction with some elements from groups 14 and 15 to form Na-M intermetallic binary compounds. These anode materials deliver high capacities from 300 to 2000 mAh g^{-1}, since a single atom can be alloy with manifold Na ions. However, large volume changes degrade the electrode and give rise to low cyclability [93]. Sn [94–98], Sb [99–101], P [102–104], Ge [105–107], Bi [108–110], Si [111–114], Pb [115], and As [116] have been investigated as anodes in SIBs.

ii) Conversion reaction electrodes react during sodiation to form new products according to: $M_aX_b + (bc){\cdot}Na \leftrightharpoons aM + bNa_cX$; where M is a transition metal and X a non-metal. Metal oxides [117], sulfides [118], selenides [119], nitrides [120], phosphides [121], and hydrides [122] have been explored for anodes in SIBs. These electrode materials also deliver high specific capacities up to 1800 mAh g^{-1}. Nevertheless, large volume expansion upon cycling, until 430% and 300% for phosphides and oxides, respectively, lead to irreversible capacity losses and low initial coulombic efficiencies [123].

iii) Organic electrodes with multielectron reversible redox reactions at C=N and C=O sites are starting to be considered in order to achieve flexible, low-cost, sustainable, and based on natural resources anodes [124,125]. Small organic molecules as disodium terephthalate [126,127], carbonyl insertion compounds [128], Schiff-base polymers [129] and polyamides [130] are being studied.

iv) Insertion or intercalation electrodes store Na ions inside their structure without disturbing their three-dimensional framework, and therefore suffering less volume expansion in comparison to alloying and conversion electrodes. The amount of intercalated sodium is determined by the thermodynamic equilibrium at the electrode/electrolyte interface and specific capacities higher than 400 mAh g^{-1} are seldom reached. Carbon based materials are the most studied insertion electrodes for SIBs because of their chemical and thermal stability and their similarity with graphite (e.g., petroleum coke [131], pitch carbon fibers [132], synthetic carbons [133], and biomass-derived carbons [134]). Among all of them, hard carbons (HCs), especially those produced from biomass wastes, are the most promising and studied material for SIBs anodes due to their high storage capacity and cycling stability, together with economic and sustainability motivations [135,136].

Hard carbons are non-graphitizable materials due to the high oxygen content and disordered structure of their precursors, whether biomass or synthetic organics. After carbonization procedures, HCs contain randomly oriented pseudographitic domains where sodium ions can be intercalated. Moreover, this carbonaceous material also contains some porosity, surface defects, and heteroatoms (N, S, P, etc.), those supply pathways for sodium

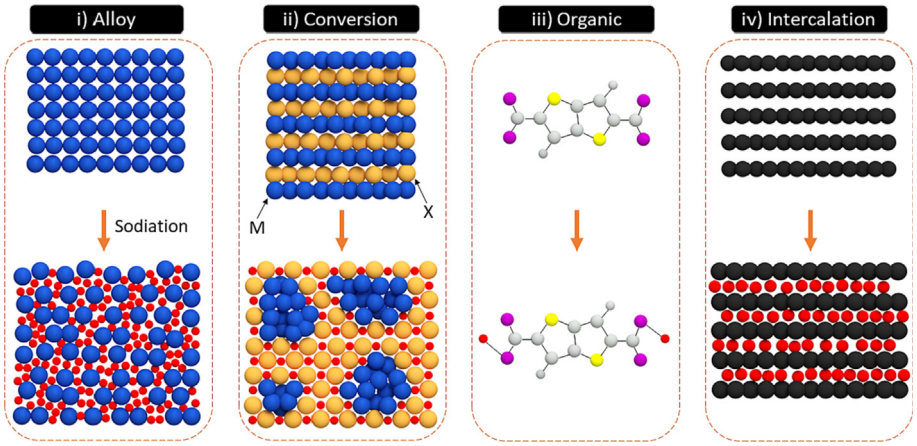

Fig. 2. Simplified scheme of the sodiation in alloy-, conversion-, organic- and intercalation-based electrodes (red spheres represent Na^+).

mobility and more sodium storage active sites. In view of the above, three different sodium storage behaviors have been reported for HCs in the literature: (i) intercalation between pseudographitic layers, (ii) adsorption on the surface edges, defects, and heteroatoms, and (iii) nanopore filling. Nonetheless, there is still a lack of consensus concerning the sodium storage mechanisms along the galvanostatic charge–discharge (GCD) voltage profiles, and six different models have been proposed: (i) insertion-filling model [137], (ii) adsorption-insertion model [36], (iii) three stage model [138], (iv) four stage model [139], (v) extended adsorption-insertion model [140], and (vi) adsorption-filling model [141]. More information on the mechanisms and the HC production (e.g., treatment temperature, porosity development, presodiation, and doping strategies) can be found in a previous review article, which focused on plant-derived hard carbon anodes for SIBs [142].

Binder compounds

Binders hold the active materials of the electrode together and fixed to the current collector, making possible the passage of electrons and therefore allowing the battery performance. Despite being only a small fraction of the anode (typically 5–10 wt%), they play an important role in the cycling stability and rate capability of LIBs and SIBs [143]. Since LIBs appeared in the market, polyvinylidene fluoride (PVDF) has been the most commonly used binder material in lab and commercial cells [144]. Besides its good adhesion properties and electrochemical stability, PVDF can absorb the electrolyte to facilitate the ion transport across the active material [143]. However, PVDF suffers severe volume expansions and partially decomposes during cell cycling, which alters the electrochemical behavior, decreases the coulombic efficiency (CE), and shortens the battery life [145,146]. Vogt et al. [147] confirmed the partial decomposition of PVDF and formation of NaF when they used 1 M $NaClO_4$/ propylene carbonate electrolyte, resulting in a lower initial CE and the early degradation of the battery performance. Furthermore, PVDF entails the use of N-methyl-2-pyrrolidone (NMP) as solvent, being toxic, expensive, environmentally unfriendly, flammable, and energy intensive to produce and recover [148].

For the above reasons, relatively low cost and environmentally benign water-soluble binders have been proposed as alternatives to PVDF. For LIBs, carboxymethyl cellulose [149,150], styrene butadiene rubber [151], poly(acrylic acid) [152], lithium polyacrylate [153], sodium alginate [154], chitosan [155], tragacanth gum [156], gelatine [157], polyethylene glycol [158], and lignin [159,160] were studied. Regarding SIBs —where PVDF decomposition can also damage the WE by separating and electrically isolating the carbon particles, resulting in lager polarization, capacity decay, and/or lower CE [144,161]— sodium carboxymethyl cellulose (Na-CMC), styrene butadiene rubber (SBR), poly(acrylic acid) (PAA), and sodium alginate (Na-Alg) have been studied so far as water-soluble alternatives (see Fig. 3 and Table 2).

(i) Na-CMC is a linear polymeric derivate of cellulose and an inexpensive and environmentally friendly material. It is synthesized by the alkali-catalyzed reaction with chloroacetic acid and mainly consists of β-linked glucopyranose residues with varying levels of carboxymethyl ($-CH_2COO^-$) substitutions [162]. Lee et al [163] showed how an increase in the degree of substitution (DS) and a decrease in the molecular weight (MW) of CMC produced lower charge transfer resistance, higher ion conductivity, better wettability with the electrolyte, and better Li^+ mobility as LIB binder. Concerning SIBs, Dahbi et al. [161] demonstrated that the use of a Na-CMC binder, for a $NaPF_6$/propylene carbonate electrolyte, improved (in comparison with PVDF) the passivation role of the solid electrolyte interface on the hard carbon (HC)-based electrode surface and therefore the cell reversibility and cyclability. Other research groups have also published promising results concerning the use of Na-CMC as a binder [164–166].

(ii) SBR is a synthetic rubber that can be used as an electrode binder in the form of aqueous emulsions, with solid contents around 50 wt%. Despite SBR can provide appropriate elasticity and flexibility, it has too low mechanical strength and its water emulsion exhibits too low viscosity to generate a sufficient coating rheology [167]. As a result, the elastic and heat-resistant SBR [168] is commonly applied in combination with the stiffer, thickener and best ionic conductor CMC. Muruganantham et al. [169] tested a Na-CMC/SBR binder in an HC anode for SIB and obtained higher initial coulombic efficiencies, reversible capacities, and rate performances than those obtained with the conventional PVDF binder. They suggested that the Na-CMC/SBR binder can promote the electrode conductivity while the PVDF-based one enhances the isolation of active materials and increases the thickness of SEI. Moreover, they noted that the water-soluble binders easily penetrated into the porous structure of carbons and contributed to improved long-term cycling stability, due to the hydrogen bonding between carboxyl groups in CMC and hydroxyl groups on the HC surface. The Na-CMC/SBR binder have also been successfully tested at several mass percentages of Na-CMC and SBR with respect to the whole electrode: 1.5:1.5 [170,171]; 3:2 [172–174]; 5:5 [175,176] and 6:4 [177,178].

(iii) PAA is a synthetic high-molecular weight polymer of acrylic acid, which was used as binder in Sn_4P_3-[179], CuP_2/C-

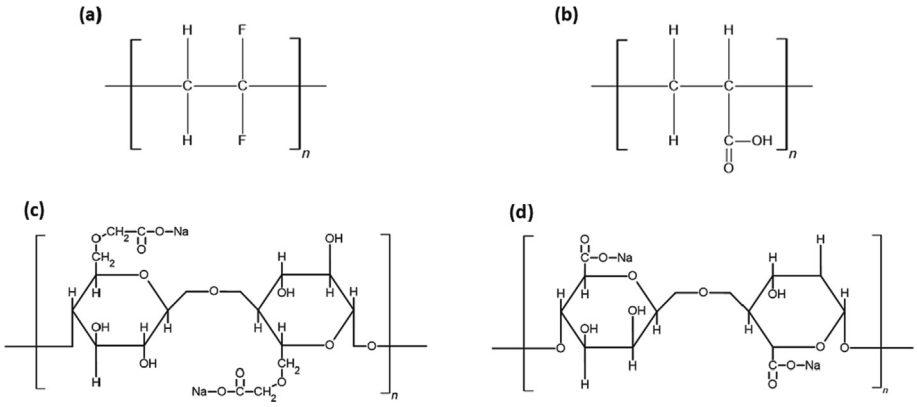

Fig. 3. Molecular structures of (a) PVDF, (b) PAA, (c) Na-CMC, and (d) Na-Alg.

Table 2
Advantages and disadvantages of the most used binders in SIBs.

Binder	Advantages	Disadvantages
PVDF	• Widely used and developed market. • High chemical and mechanical stability.	• Volume expansion, partial decomposition, and carbon particles isolation during SIB cycling. • NMP as solvent: toxic, expensive, environmentally unfriendly, and flammable. • Controlled manufacturing to avoid vapor dispersion and recovery system to recycle the solvent.
Aqueous binders	• Environmentally benign, can be employed in air, and no solvent recovery is required.	
Na-CMC	• Inexpensive and derived from cellulose. • Good adhesion and ionic conductivity. • Improved electrode cyclability.	
SBR	• High elasticity and thermal stability. • The mixture Na-CMC/SBR enhances the binder properties.	• Low mechanical strength and viscosity.
PAA	• Good adhesion and electrode cyclability	
Sodium alginate	• More polar than Na-CMC: higher interfacial interactions and adhesion. • Natural polymer.	
Free binder electrodes	• Higher electronic conductivity and ionic diffusion. • Enhanced energy density and cycling stability.	• Early stage of development. • Template-assisted methods or other advanced techniques (e.g., electrospinning) are usually required.

[180], FeP-[181], and Sb-based anodes [51,101]. Similar to Na-CMC, PAA forms strong hydrogen bonds with the active materials and current collectors due to the availability of carboxylic acid groups [182]. Other authors also used its sodium salt (Na-PAA) as binder for black phosphorus-[104], Sn-[97], and iron phosphide-based [183] anodes. Fan et al. [184] employed Na-PAA with N-doped hollow carbon nanotubes and obtained better results —compared with the traditional PVDF binder— in terms of electrochemical activity, internal resistance and SEI homogeneity. Darjazi et al. [185] assessed the influence of various water-soluble binders for a coffee ground-derived HC and they found PAA better than CMC and PVDF in terms of reversible capacity and capacity retention after 100 cycles, only surpassed by the alginate binder.

(iv) Na-Alg is the sodium salt of the natural polysaccharide alginic acid. Na-Alg is extracted from brown algae and also contains carboxylic groups in each of the polymer's monomeric units. De la Llave et al. [186] obtained similar performances for Na-CMC and Na-Alg binders for hard carbon anodes, reporting a stable and constant capacity value in SIBs for more than 250 cycles, much higher than those obtained with a PVDF binder. On the other hand, Hwang et al. [17] stated that Na-Alg is more polar than Na-CMC and provides better binder/particles interfacial interactions and a stronger electrode/collector adhesion. Na-Alg binder properties were tested for HC electrodes and several papers have been published since 2018 [187–192].

Regardless of the material finally chosen, it should be noted that binders may reduce the ionic diffusion by decreasing the electronic conductivity and blocking HC pores, since binders are usually insulating and electrochemically inactive materials. As an alternative, binder-free or self-supported electrodes are emerging to improve the electronic conductivity as well as the energy and power densities. Recently, a hard carbon self-supported electrode was prepared through simple impregnation of cellulose and cotton filter papers with a phenolic resin solution, prior to a mechanical pressing and subsequent carbonization [193]. Binder-free electrodes were also produced from carbonized-leaf membranes [194] and wood carbon [195]. However, the development of binder-free electrodes is at an early stage and to our knowledge, no more plant-derived HC self-supported electrodes have been tested in SIBs. Additional information about binder-free electrodes for sodium-ion batteries is available in a previous review [196].

2.6. Reference electrode

When current flows through the electrochemical cell, one of the electrodes should remain practically constant in order to have a well-defined potential reference value to measure or control the potential of the electrode under investigation [13]. For this purpose, a good reference electrode (RE) must be non-polarizable, reproducible, and stable during all electrochemical measurement

length. In essence, the RE must act as a spectator that observes one point in the current line distribution between the WE and the CE without altering the cell performance [197–199].

Taking a look back at LIBs setups, lithium metal has been the most used reference electrode material [200]. However, it cannot be considered a suitable RE because of the irreversibility of its reactions [201]. Potential deviations are generated from the reactions between the active metal and solution species that change the passivation layer on the Li surface [86,202]. As a solution, metallic alloys and insertion materials have been studied to replace Li reference electrodes. Alloy materials such as Li-Sn [200,203,204], Li-Al [205,206], Li-Bi [198], and Li-Au [30,207] show relatively stable potentials and allow the use of metallic wires that can be lithiated in-situ to form the alloy at its surface. Care must be taken because dealloying of RE and the consequent potential drift can occur over time [30]. Insertion materials as lithium titanium oxide ($Li_4Ti_5O_{12}$) [208–212] and lithium iron phosphate ($LiFePO_4$) [199,213] give two-phase reactions upon intercalation or deintercalation with lithium. Since they operate within the stability window of most electrolytes, a passivation free surface and high potential stability are achieved [26,199]. Finally, quasi-reference (QREs) or pseudo-reference electrodes (PRE), which consist of a simple metal wire, do not show a suitable behavior in LIBs due to electrochemical changes at its surface during cell operation [201,214].

Back to SIBs, sodium metal is the commonly used RE [215–218], despite having shown to be unstable and poorly reproducible [85]. As previously mentioned, the generation of an unstable SEI on sodium metal surface causes impedance increasing and unreliable voltage measurements [219]. Moreover, a signal associated with electroactive degradation products can result in erroneous interpretations when they are confused with the intercalation reactions inherent to the WE [220]. Despite the widespread use of metallic sodium, silver wire [221] and activated carbon [28,85] were investigated as pseudo-reference electrodes. Recently, Linsenmann et al. [170,171] designed a micro-reference electrode for SIBs based on an in-situ sodiated 50 μm tin-coated copper wire, with a potential stable enough to allow in-situ Electrochemical Impedance Spectroscopy. More information about reference electrodes performance in SIBs is provided in Section 5.

2.7. Electrolyte

The selection of the electrolyte is a key point to achieving a satisfactory SIB performance. As previously mentioned, a solid electrolyte interphase (SEI) appears on the negative electrode due to the electrolyte components decomposition. SEI controls the reversibility and kinetics of sodium insertion into hard carbon electrodes while the solid permeable interface (SPI) also affects the cathode surface. Since different behaviors in SEI solubility and mechanical properties between LIBs and SIBs exist [89,90,222], research is required to select proper electrolytes for SIBs to achieve: (i) high ionic and no electronic conductivity; (ii) wide electrochemical stability window (the potential region where no considerable electrochemical oxidation–reduction of the electrolyte takes place [18]); (iii) no reactivity with cell components (separator, binder, collectors, etc.), (iv) wide thermal stability window, and (v) low toxicity, environmentally friendliness and low cost [19,223].

2.7.1. Alkyl carbonate-based electrolytes

Most liquid electrolytes in SIBs consist of sodium perchlorate ($NaClO_4$) or sodium hexafluorophosphate ($NaPF_6$) salts dissolved in carbonate ester-based solvents. Carbonates can be linear, such as diethyl carbonate (DEC) and dimethyl carbonate (DMC), or cyclic, like propylene carbonate (PC), ethylene carbonate (EC), and butylene carbonate (BC). In most cases, 1 M salt concentration is dissolved in a pure carbonate solvent (or binary mixtures of carbonates). Moreover, other salts as sodium bis(fluorosulfonyl)imide (NaFSI), sodium bis(trifluoromethylsulfonyl)imide (NaTFSI) and sodium trifluoromethanesulfonate (NaOTf) have also been investigated [224–227].

Sodium perchlorate ($NaClO_4$) was the first and up to now the most widely used salt for SIB electrolytes. However, it is known that an unstable SEI appears when $NaClO_4$ is used in combination with alkyl carbonates [228]. Moreover, Kumar et al. [229] found a continuous growth of SEI associated with the high reduction potential and low barrier for the ring-opening of EC. As a potential improvement, several studies showed how fluorinated electrolytes give rise to a more stable SEI, best electrode kinetics and higher conductivity. Fluorinated compounds produce NaF on the electrode surface, which has low solubility in an aprotic solvent and hinders the electrolyte decomposition. That is why $NaPF_6$-based electrolytes supply better HC electrode reversibility and cyclability [230].

Pan et al. [231] reported that NaF together with sodium ethylene decarbonate (SEDC) were the main components of the SEI layer in a HC-based anode when 1 M $NaPF_6$ was used. Sodium alkyl carbonates, sodium carboxylate, Na_2CO_3, and $Na_xPF_yO_z$ were also detected in lower concentrations. Based on the influence on SEI, the suitability of $NaPF_6$-based electrolytes was also confirmed by Bhide et al. [18] and Lee et al. [232], who observed that $NaPF_6$ in EC:DMC provided better HC electrode kinetics than $NaClO_4$ or $NaCF_3SO_3$ salts.

Regarding the possible effects of solvent, Ponrouch et al. [19] found much higher ionic conductivity for mixtures than for single solvent-based electrolytes in the following descending order: EC:DMC, EC:PC, EC:DEC, PC, DMC, and DEC. Moreover, after evaluating the suitability of several salts and solvents, they identified the mixture of 1 M $NaPF_6$/EC:PC as the optimum selection. One year later, Zhao et al. [233] reported better HC capacity retention and thermal stability when $NaPF_6$ was used in EC:DMC solvent instead of PC. It must also be considered that, according to Jang et al. [234], DEC can be unstable in contact with Na metal.

Chen et al [235] recently analyzed the effect of Na salts and carbonate-based solvents on the electrochemical performance of HC electrodes, by comparing the use of 1 M $NaClO_4$, $NaPF_6$, NaTFSI, NaFSI, or NaOTf salt in EC:DEC, EC:DMC, and EC:PC binary solvents (1:1 v/v). They observed that 1 M NaTFSI/EC:DMC, closely followed by $NaPF_6$/EC:DCM, as the best electrolyte formulation in terms of initial coulombic efficiency (ICE), reversible capacity, and electrochemical stability (For more information see Section 5.1, entitled "Fundamental electrochemical concepts"). Hence, fluorinated salts solved in EC:DMC mixtures seem to be the best electrolyte candidates for SIBs.

2.7.2. Electrolyte additives

The addition of additives to alkyl carbonate-based electrolytes is a growing strategy to improve SIBs performance. Komaba et al. [48] in 2011 were the first to test conventional LIBs electrolyte additives in SIBs. They evidenced how fluoroethylene carbonate (FEC) in 1 M $NaClO_4$/PC electrolyte improved the reversibility of the electrochemical sodium insertion in an HC anode. Conversely, difluoroetyhene carbonate (DFEC), vinylene carbonate (VC), and ethylene sulfite (ES) additives did not work properly. The suitability of FEC addition was later confirmed in $NaPF_6$-based electrolytes, improving the anode performance due to the suppression of electrolyte decomposition and the lower electrode/electrolyte interphase resistance of the formed SEI [186,230,236]. Moreover, Bouibes et al [237] found that there was an optimum value for the FEC concentration, from which SEI became unstable. Recently, Fondard et al. [226] studied the addition of FEC when $NaPF_6$ or NaTFSI salts in EC:DMC were used as electrolyte. They reported

that using a 3 wt% FEC-containing electrolyte improved the overall cell capacity and coulombic efficiency. The authors suggested that SEDC available in the SEI played a beneficial role in its physicochemical properties, while NaF (more abundant when using FEC) limited SEDC solubility and improved Na^+ conduction through the SEI.

Interaction between binder and electrolytes must also be considered. For instance, Dahbi et al. [161] observed that the addition of FEC (2 vol%) to 1 M $NaPF_6$/PC in an HC half-cell had a positive effect when PVDF binder was used, but negative when the binder was Na-CMC. Finally, it is worth mentioning that the following alternative additives are in the spotlight: succinic anhydride [238], adiponitrile (ADN) [166], prop-1-ene-1,3-sultone (PST), and 1,3,2- Dioxathiolane-2,2-dioxide (DTD) [239].

2.7.3. Other electrolytes

Nonfluorinated, ether-based, ionic liquids and aqueous electrolytes are emerging alternatives that try to compete with the better-known alkyl carbonate-based electrolytes (see Table 3).

(i) Nonfluorinated electrolytes. Since fluorinated compounds are toxic and undesirable according to the green chemistry principles, fluorine-free electrolytes are being studied. Recently, Morikawa et al. [164] found 0.5 M sodium tetraphenylborate ($NaBPh_4$) in 1,2-dimethoxyethane (DME) as a stable electrolyte for hard carbon anodes. Also, nonflammable solvents as trimethyl phosphate (TMT) are being considered [51].

(ii) Ether-based electrolytes. Glyme-based electrolytes have gained growing interest because ethers allow the intercalation of solvated sodium ions into graphite anodes. It is a reversible process called "co-intercalation reaction" that shows suitable reversibility at low overpotentials and high power performance, though limited capacity [240–244]. Moreover, ether-based electrolytes as glyme, diglyme and tetraglyme are starting to be considered as solvent candidates for HC-based SIBs [245–249]. Ether-based electrolytes were proven to form thinner and more compact SEI layers than the ester-based ones, providing higher ICE, even when carbon materials with high surface areas were tested [249–251].

(iii) Ionic liquids (ILs). Using ILs as electrolytes for SIBs, although in an incipient state, is growing due to their high conductivity, environmental compatibility, and high thermal stability. ILs are molten salts formed by an organic cation (mainly imidazolium or pyrrolidinium) and delocalized anions such as $[FSI]^-$, $[TFSI]^-$, tetrafluoroborate $[BF_4]^-$, hexafluorophosphate $[PF_6]^-$, hexafluoroantimonate $[SbF_6]^-$, or trifluoroacetate $[TFA]^-$ [252,253]. Indeed, the same salts used with Alkyl carbonate-based electrolytes can be employed in ILs electrolytes, as $NaClO_4$ [254], $NaPF_6$ [255], or $NaBF_4$ [256], being NaFSI [257–259] and NaTFSI [260–262] the most studied to date.

(iv) Aqueous rechargeable sodium ion batteries (ASIBs) with high ionic conductivities are being also investigated to solve the organic electrolytes safety problems (toxicity and flammability). However, aqueous batteries are challenged by the narrower thermodynamic voltage window (1.23 V) and the subsequent lower energy density [263]. Moreover, other parasitic reactions are also involved (H_2/O_2 evolution, electrode materials dissolution, hydrogen co-intercalation, etc.) as well as the cell pressure increasing due to the water decomposition [264]. These impediments can be mitigated by using the highly concentrated **"water-in-salt" (WIS) electrolytes**, which strongly suppress the water activity and allow to increase the stable operation window up to ~3.0 V. In these electrolytes, with salt/water mass or volume ratios higher than 1, all the water molecules are involved in the ion solvation shells, so no "free" water is available [265]. Moreover, as in ILs, the same salts used in the common organic electrolytes can be selected, being $NaClO_4$ widely studied due to its high solubility and the wide electrochemical window of the resulting electrolyte [266,267].

(v) SEs and GPEs. Solid-state electrolytes (SEs) act simultaneously as the ion transport medium and the separator, avoiding dendrite formation, fire or explosion possibility, and side reactions existing between liquid-phase electrolytes and electrodes. Polyethylene oxide (PEO) is the most studied polymer and has been investigated in combination with several salts, e.g., $NaClO_4$ [268], $NaPF_6$ [269], NaFSI [270], and NaTFSI [271]. Inorganic fillers as SiO_2 [271], TiO_2 [272], and Al_2O_3 [273] can be added to facilitate the ion conduction and improve the performance of SEs. Nonetheless, high interface resistances and low ionic conductivity ($<10^{-4}$ S cm^{-1} at room temperature) force to work at temperatures above 60 ℃ [274]. As an alternative to SEs, gel-polymer electrolytes (GPEs) are composed of liquid plasticizers, allowing better interfacial contact with the electrodes and higher ionic conductivities. Polymer matrixes as poly(ethylene oxide) (PEO) [275], poly(vinylidene fluoride-co-hexafluoropropylene) (PVDF-HFP) [276], and polyacrylonitrile (PAN) [277] have been used in conjunction with salts and ester, ether or ionic solvents. More information on this innovative technology is available in previous reviews [274,278–280].

3. Carbonaceous electrode preparation for lab scales

To make a functional hard carbon working electrode, active materials need to be mixed with additives and binders to produce a plane compact electrode and increase its conductivity, elasticity,

Table 3
Main properties of different electrolytes used in SIBs.

Electrolyte	Advantage	Disadvantage
Carbonate esters	• Wide electrochemical stability and wide industrial use. • Fluorinated salts solved in EC:DMC seems to be the best combination for SIBs. • Additives (as FEC) can improve the cell reversibility.	• Toxicity and flammability. • SEI instability.
Ethers	• Thinner and more stable SEI layer: higher ICE and long-term cycling.	
ILs	• High conductivity, thermal stability, and environmental compatibility. • Low vapor pressure and high boiling points.	• Incipient state and cost challenges. • Higher temperatures may be required to avoid ion transport issues.
ASIBs	• No toxic or flammable.	• Low voltage window (1.23 V) and parasitic reactions.
WIS	• No toxic or flammable. • Increased voltage window (~3.0 V).	• Preliminary stage.
SEs	• High safety and energy density. • Not SEI or side reactions.	• High cell working temperatures are required to balance the low wettability and ionic conductivity.
GPEs	• Better interfacial contact and ionic conductivities. • High working temperatures are not required.	

and viscosity. Inherited from LIBs technology, PVDF, NMP, and black carbon are still usually added as binder, solvent, and conductive agent, respectively. A common initial weight ratio of active-material:carbon-black:binder is 8:1:1 [281], although these ratios should be modified as a function of the properties of the active material. As discussed previously, alternative water-soluble binder compounds can be selected. Moreover, the addition of carbon black can be avoided to increase the energy density of the composite electrode. In this respect, lignin-derived HC produced at high temperatures exhibited similar electronic conductivity to acetylene black [139].

In order to properly prepare a slurry mixture —containing the active material, additive, binder, and solvent— several techniques have been proposed, including planetary mixing, magnetic stirring, vortex or even ultrasonication. At this point, it should be noted that preparing uniformly dispersed solutions of green water-soluble binders requires bigger mechanical efforts than PVDF in organic solvents. Therefore, to obtain suitable and homogeneous slurries, a first mixing step (e.g., Na-CMC and water) is desirable prior to adding the active material to avoid lump formation. Once a carbonaceous homogeneous slurry is obtained by agitation, the mixture needs to be deposited on the current collector (e.g., aluminum foil) and extended using a doctor blade or a baker applicator to obtain a thickness-controlled composite electrode (see Fig. 4). Previously, the metal foil collector has to be spread and bonded onto a glass plate with the help of a small amount of water or other solvents. To obtain a completely flat surface, air bubbles can be removed by rubbing the metal foil with a dry paper towel or a cotton swab. Finally, the copper or aluminum surface should be cleaned (e.g., with acetone or ethanol) to remove any trace of oil or other manufacturing pollutant.

After coating the anode slurry, quickly drying is advisable because slurry components can be segregated according to their density and give rise to a non-uniform film. A laboratory heating plate at 100 °C can be used until the solvent evaporates. Additionally, the foil can be pressed with a compression roller to obtain a more compact anode [282]. From this point, the anode can be cut out to the desired shape using scissors (rectangular) or a puncher (circular) and be dried at 100–120 °C overnight, usually under vacuum, to evaporate solvent residues. Finally, the resulting anodes can be weighted, wrapped, and placed into a glove box, where the battery will be assembled under an inert atmosphere (i.e., H_2O and O_2 concentrations below 0.1 ppm).

4. Types of cells

Several electrochemical setups are available for battery assembly. Beaker, coin, and Swagelok-type cells are the three most used configurations for testing electrodes at the lab scale (see Fig. 5).

(i) Beaker cell is the simplest assembly system and consists of a glass filled with the electrolyte, in which the electrodes are inserted. This setup facilitates the use of a third electrode by allowing the use of large REs such as the junction reference electrode.

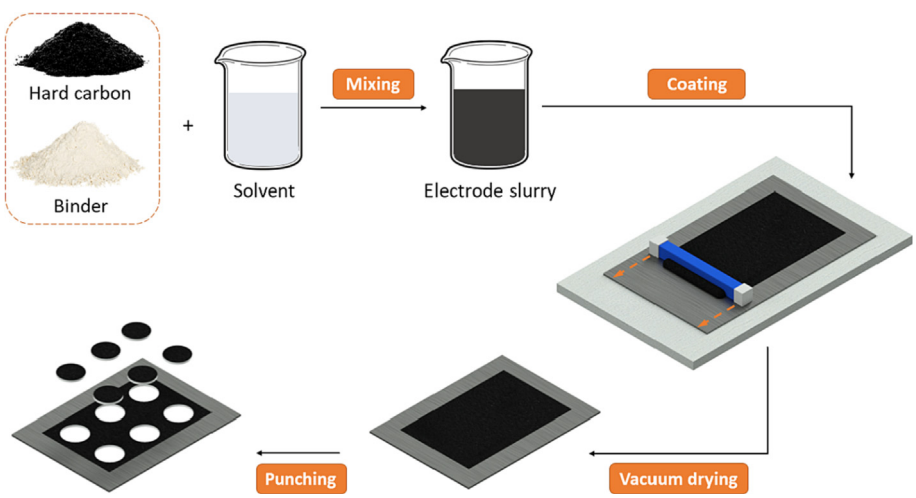

Fig. 4. Simplified scheme of the hard carbon electrode manufacturing procedure.

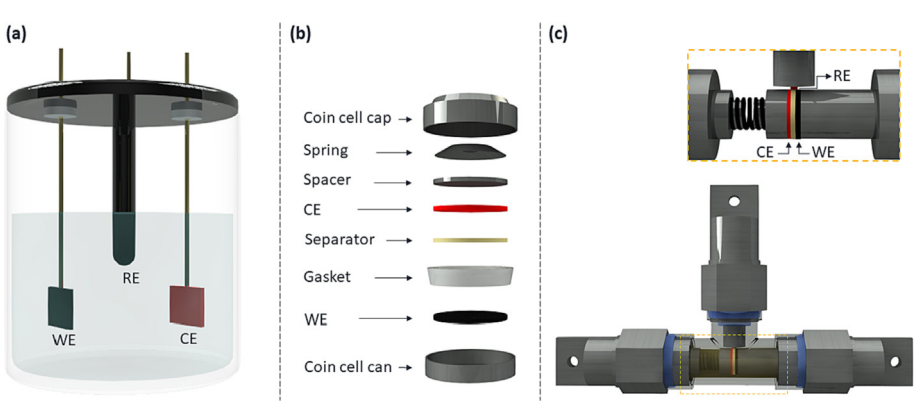

Fig. 5. Lab-scale configurations used to measure the performance of anodes in SIBs: (a) beaker cell, (b) coin cell, and (c) Swagelok T-cell.

However, the beaker cell involves several disadvantages, such as the high amount of electrolyte required, the absence of stack pressure between the electrodes, possible evaporation of solvents during testing, and the need to keep the cell in a glovebox for the whole duration of the experiment [26].

(ii) Coin cells are commercially available batteries, whose parts can be purchased to test new materials. This setup has been the most popular in LIBs studies for the last 30 years [281] and their benefits may be summarized as follows: fast and simple assembly, good reproducibility, small amounts of active material are required, and, due to their small size, several cells can be tested simultaneously [283]. There are many types of coin cells, and their code (e.g., CR2016) indicates the diameter (20 mm) and the thickness (1.6 mm). A coin cell is composed of bottom and top cap, polypropylene gasket for electrical insulation and air tightness, spacer, and wave spring to put pressure on electrodes (see Fig. 5b). Between the bottom cap and the spacer, anode, separator, electrolyte, and cathode must be inserted/injected before sealing the coin cell using a specific crimping machine. This operation has to be carried out inside a glove box and the assembled cells should be at room temperature for several hours before testing to ensure that electrolyte penetrates into the electrodes and separator [281]. In front of their advantages, the thin metal cell casing can be deformed and make it difficult to achieve the desired pressure on the electrodes [22]. Moreover, coin cells are designed to work as two-electrode systems, thus attaching a reference electrode is not an easy task (see Section 5.5 for further details).

(iii) Swagelok-type cells use gas tubing union fittings as housing and two metallic plungers (made of stainless steel or aluminum) as current collectors [284,285]. The popularity of this setup is due to its easy construction, good gastight sealing and low cost. Counter and working electrodes, separator, and electrolyte are placed inside the Swagelok fitting and then the cell is sealed by pressing the plungers with PTFE ferrules. Pressure on electrodes is maintained by an internal compression spring. An insulator is also required to avoid short circuit because of contact between plungers and the cell body. A plastic tape (PTFE) can cover the plungers [27] or a plastic tube can be placed inside the cell body to cover the electrodes [170]. As shown in Fig. 5(c), three-electrode systems can be easily built by replacing the straight union with a tee union fitting and adding a third plunger [286,287], being this the most commonly used three-electrode configuration [27]. Usually, a sodium metal disc placed perpendicularly to the working and counter electrodes is used as the RE [18,19,226,288]. However, and as shown in Section 5, alternative RE configurations, such as those based on metallic wires [170] and sodium metal rings [89] have been proposed.

(iv) Other cells. Once the electrochemical properties of electrodes have been tested, the next step is to check their performance in larger electrochemical batteries, such as cylindrical, prismatic and pouch cells [289]. Pouch cells, in which the electrodes are stacked and sealed by a flexible foil, are the most employed in SIBs research [43,290]. Additionally, several cells have been developed to allow in situ/in operando characterization techniques, such as X-ray diffraction or absorption [291,292], UV − visible spectroscopy [293], infrared spectroscopy [294], mass spectrometry [295] and nuclear magnetic resonance [296]. Furthermore, some companies sell tailor-made lab-scale setups to check the electrochemical capacities of materials. Two or three electrodes-based setups are available; however, few studies using them have been published so far [208,213,293,297].

5. Electrochemical techniques

Fundamental knowledge of electrochemical techniques is required to properly evaluate the electrochemical performance of active materials in terms of capacity, kinetics, and cycling stability. Potentiostat/galvanostat instruments are used for this purpose, given their ability to conduct accurate measurements across relatively wide current and voltage ranges. In the following paragraphs, the most commonly used electrochemical measurement techniques are introduced in order to better understand the electrochemical data acquired in battery research.

As discussed in previous sections, the configuration of an electrochemical cell consists of three electrodes: the working electrode (WE), a counter or auxiliary electrode (CE) and a reference electrode (RE). With this in mind, there are two basic techniques to investigate SIBs by imposing large perturbations that drive the electrode to a condition far from equilibrium [197]: controlled-potential and controlled-current techniques (see Fig. 6a and b). In the controlled-potential or potentiostatic control, the current (i) between WE and CE is adapted to obtain the desired constant potential difference (E) between WE and RE. The resulting current between WE and CE is registered as a function of time [$i(t)$] or potential [$i(E)$]. In the controlled-current or galvanostatic control, a current value is fixed and applied between WE and CE, while the resulting potential difference between WE and RE is measured and recorded versus time or current.

5.1. Fundamental electrochemical concepts

Before going into techniques, a brief explanation of some basic concepts is needed. The theoretical specific capacity (Q_t) of an electrode material is one of the most influential parameters and is given by the Faraday's law given in Eq. (1), where n is the electron-transfer number, F is the Faraday constant (96,485 C mol^{-1}), and M_w (g mol^{-1}) is the molecular weight of the anode material [298]. Moreover, during the course of an experimental measurement, the specific capacity (Q) can be obtained under galvanostatic charge/discharge by means of Eq. (2), where i is the charge/discharge current, Δt is the charge/discharge duration, and m is the mass of active material. Specific capacities are conventionally expressed in mAh g^{-1} [299].

$$Q_t = \frac{nF}{3.6\,M_w} \tag{1}$$

$$Q = \frac{i\Delta t}{3.6\,m} \tag{2}$$

$$\varepsilon = \frac{i}{3.6m}\int_{t_1}^{t_2} V(t)\mathrm{d}t \tag{3}$$

The gravimetric energy density (ε), which is also a key parameter to producing competitive full cells, can experimentally be calculated from Eq. (3) [299], where $V(t)$ is the voltage that changes over time under galvanostatic charge or discharge. Electrodes with high specific capacities are required to achieve high energy density cells. Moreover, energy density can further be improved by widening the voltage window of the cell. The volumetric energy density (u) is also relevant since battery size is a determinant market factor.

The coulombic efficiency (CE) is defined as the ratio between the cell discharge capacity and the cell charge capacity within the same cycle [13]. Hence, CE is the ratio between the total amount of Na ions back to the cathode and the total amount of Na ions previously delivered from it. When CE refers to the first charge–discharge cycle is known as the initial coulombic efficiency (ICE), widely used to quantify the loss of charge capacity due to SEI formation and other Na^+ irreversible trapping phenomena. It should be noted that current density is often expressed as a C-rate, where 1 C corresponds to the required current to fully charge

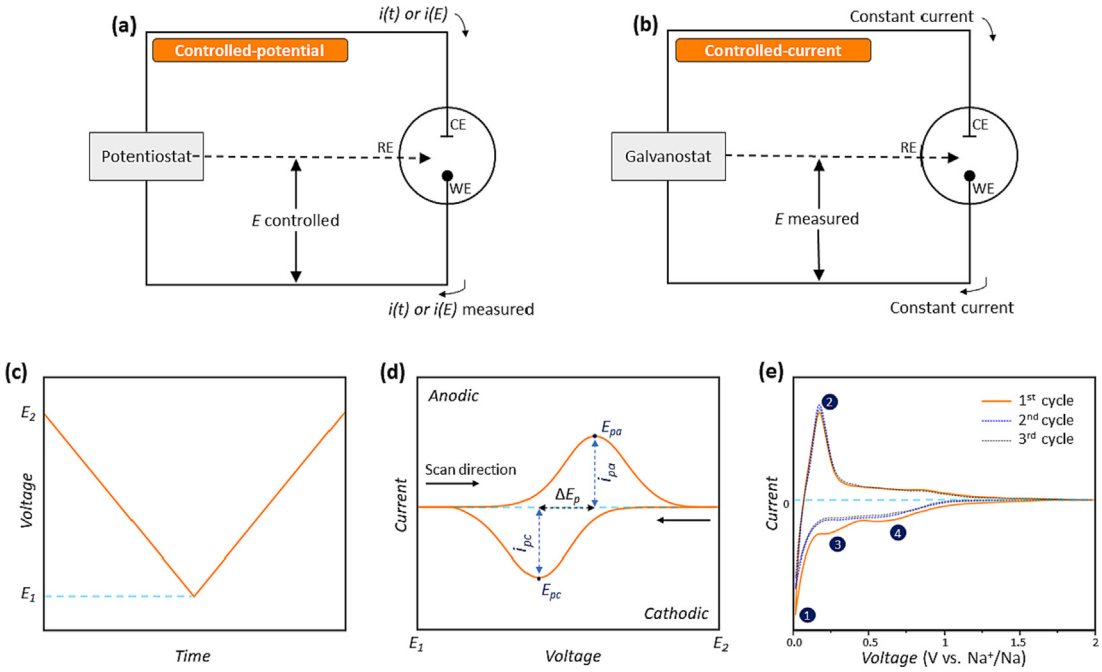

Fig. 6. Potentiostatic (a) and galvanostatic (b) control configurations. Plots obtained from a CV experiment: (c) applied voltage profile, (d) current response vs. voltage and related parameters, and (e) an example of current response shape for a hard carbon electrode in a SIB.

or discharge the battery in 1 h. Even though the specific capacity can strongly vary as a function of the tested active material, 300 mAh g^{-1} is commonly chosen as reference value. In this case, a 0.1 C rate (which is usually adopted in electrode testing) corresponds to a specific current of 30 mA g^{-1}.

It should also be kept in mind that two different kinds of processes can take place at the tested electrode: faradaic and nonfaradaic. The former comprises reactions in which electrons are transferred across the interface between the electrode and the electrolyte. This phenomenon causes reduction or oxidation of the electrode and receives its name since those reactions are governed by the Faraday's law. On the other hand, nonfaradaic or capacitive processes take place when no charge-transfer reaction occurs, but there is an accumulation of charges at the electrode-solution interface because of the electrical double layer formation [197]. Batteries operate on faradaic processes to provide high energy density (i.e., electrochemical reactions on the electrode surface and intercalation of ions in the bulk). Conversely, carbon-based supercapacitors (or electric double-layer capacitors) use the non-faradaic double-layer capacitance to deliver high power for short times [300].

5.2. Potentiodynamic techniques

Cyclic voltammetry (CV) is a potentiodynamic technique commonly used for understanding the processes occurring in an electrode. A potentiostat is used to control the applied potential between the WE and the RE. Three parameters need to be selected: the terminal voltages (E_1 and E_2) and the scan rate (v). Thus, a triangular voltage profile is applied to the cell as shown in Fig. 6(c). Terminal voltages and scan rates can be established according to the following criteria [301]: (i) reactions at the electrode have to take place in the chosen voltage range and, at ending points, current must tend to zero; and (ii) the experimental capacity obtained at the selected scan rate has to be similar to the theoretical capacity of the electrode material. Generally, for Na-ion half-cell systems, the scan rate is set between 0.1 and 10 mV s^{-1} and the voltage window between 2 and 3 V for E_1 and 0.01 V for E_2 (vs. Na/Na^+).

A typical cyclic voltammogram is shown in Fig. 6(d), where peak voltage (E_p) and peak current (i_p) can be identified. It should be noted that subscripts a and c mean anodic and cathodic, respectively. Care must be taken when interpreting cyclic voltammograms, since two different conventions can be adopted: (1) the IUPAC approach, according to which the anodic currents are plotted upward along the vertical axis and more positive (anodic, oxidizing) potentials are plotted to the right along the horizontal axis (as shown in Fig. 6d); and (2) the polarographic convention, which plots the cathodic currents upward and more positive potentials to the left [302]. It is important to highlight that sodiation and desodiation of hard carbon electrodes correspond to the cathodic and anodic curves, respectively.

Cyclic voltammograms provide qualitative information about reversible and irreversible reactions taking place in the WE across cycles. Fig. 6(e) shows a typical current response and the characteristic peaks for an HC-based electrode cycled in a SIB half-cell. The sharp cathodic peak near 0 V (point 1) and its analogous anodic peak (point 2) are ascribed to the reversible insertion/extraction mechanisms of Na^+ [139,303,304]. Moreover, cathodic peaks between 0.2 and 1 V appear in the first discharge cycle (points 3 and 4) but fade during the subsequent cycles. These irreversible peaks are attributed to the electrolyte decomposition to originate the solid electrolyte interface (SEI), as well as to the irreversible Na^+ trapping into HC defects and surface functional groups [305,306]. In other words, the less irreversible area in the first cycle, the better initial coulombic efficiency. Likewise, overlapped CV profiles in next cycles reveal high-capacity retention of the studied anode.

CV is also employed to estimate the diffusion-controlled and pseudocapacitive contributions to current response. The total stored charge in an electrode is composed of (1) the faradaic contribution from the Na^+ intercalation in the electrode bulk, (2) the faradaic contribution from the charge-transfer process in the electrode surface, known as pseudocapacitance, and (3) the nonfaradic contribution from the double layer effect [307]. The current

response of the electric double layer (i_{dl} in Eq. (4)) is analogous to a physical capacitor. For its part, i_{dl} is only determined by its capacity (C) and the scan rate (v) and, in batteries, its value is very small [301].

$$i_{dl} = C\frac{\partial E}{\partial t} = Cv \tag{4}$$

$$i_F = i_S + i_B = k_1 v + k_2 v^{1/2} \tag{5}$$

$$i_s = a v^b \tag{6}$$

$$\frac{i_F}{v^{1/2}} = k_1 v^{1/2} + k_2 \tag{7}$$

The faradic current (i_F) can be divided as the related with the pseudocapacitive reactions on the surface (i_s) and the associated with the reactions in the electrode bulk (i_B). Since the diffusion of charge carriers (Na^+) is much slower inside the solid electrode than in the liquid electrolyte, i_s and i_B show different responses vs. the scan rate. The current from the pseudocapacitive mechanism is proportional to scan rate, as well as a physical capacitor. Meanwhile, the current response from the bulk contribution is linearly proportional to the square root of the scan rate (Eq. (5)). In the literature, the pseudocapacitive contribution is commonly obtained from the power law shown in Eq. (6). By measuring how the current (i) changes with the scan rate at a fixed potential, the b parameter can be calculated from the slope of the log i vs. log v plot. Given the above, b values of 0.5 and 1.0 indicate pseudocapacitive and diffusion-controlled current response, respectively [308]. However, although this procedure allows knowing what process dominates the system, the numerical contribution of each mechanism cannot be obtained. As a solution, Dunn's group [307,309] proposed a method to quantify k_1 and k_2 from Eq. (5) at given potentials. Once rearranged to Eq. (7), by representing $i/v^{1/2}$ in the y-axis and $v^{1/2}$ in the x-axis, k_1 can be determined from the slope and k_2 from the y-axis intercept point of the fitted straight line, respectively.

5.3. Galvanodynamic techniques

Galvanostatic charge–discharge (GCD) is the preferred method to evaluate the capacity and reversibility of electrode materials. Opposite to CV, a constant current is applied between the WE and the CE until the terminal voltage is reached; then, the current direction is inverted as shown in Fig. 7(a). Usually, a small current (e.g., 0.1 C) is selected to prevent or reduce the polarization of the electrodes (see Section 5.5.1). Terminal voltages for half-cells, analogous to CV, are typically around 0.01 V for the bottom voltage and between 2 and 3 V for the upper voltage. Attention should be given to low voltages (near 0.0 V vs. Na/Na^+) since hard carbons can exhi-

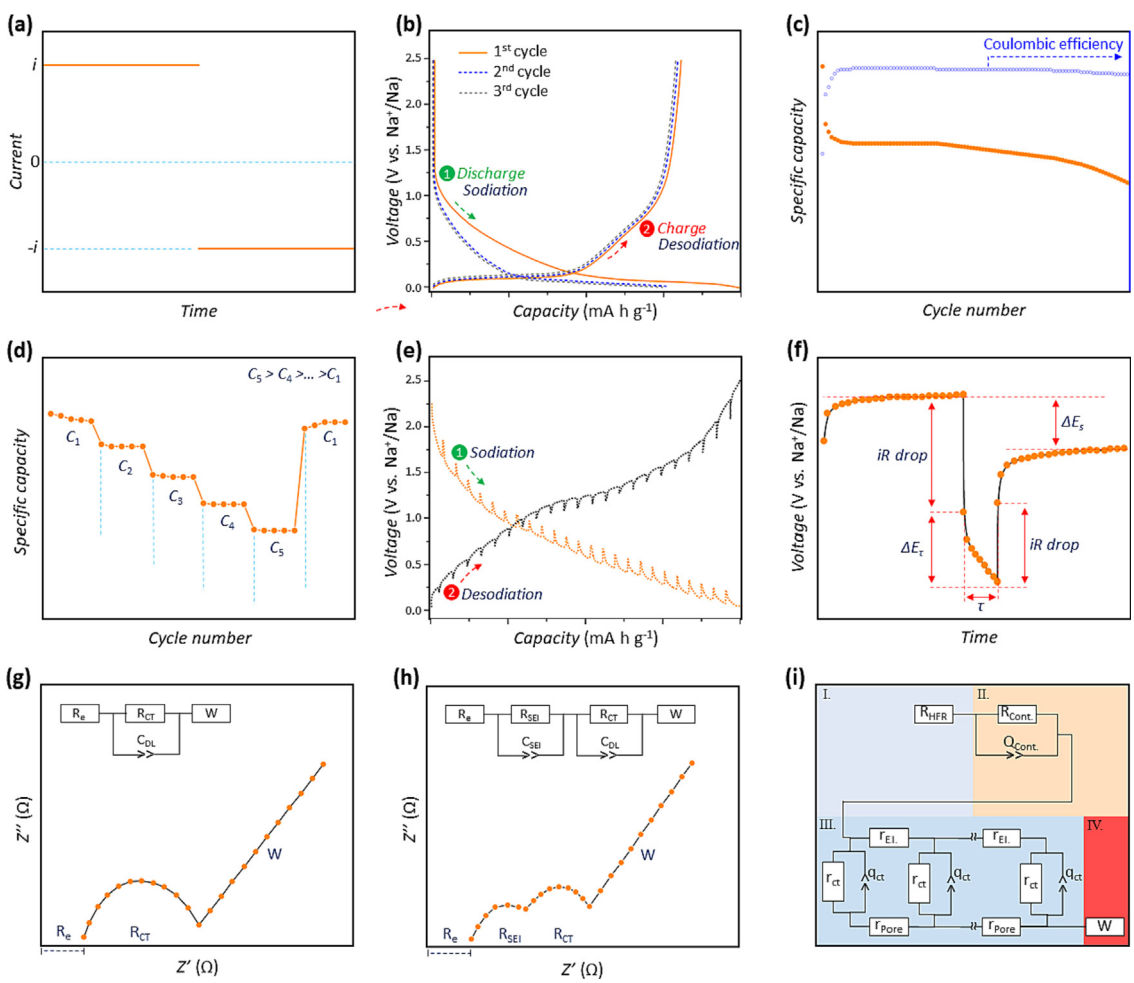

Fig. 7. Plots obtained from a GCD experiment: (a) applied current profile, (b) typical voltage response for hard carbon electrode, (c) cycle stability illustration, (d) rate capability behavior, (e) GITT curve, and (f) parameters from GITT curve in a selected rest-discharge-rest period. Typical plots from an EIS measurement: (g) Nyquist plot for a Randles equivalent circuit, (h) Nyquist plot for an SEI-added Randles equivalent circuit, and (i) TLM-based equivalent circuit. Reproduced from Ref. [348] with permission from IOP Science.

bit a flat potential plateau, which potentially may cause dendrites. In this line, Wang et al. [310] found how sodium metal begins to plate on the surface of a kelp-derived HC at −0.0052 V vs. Na/Na^+.

Galvanostatic charge/discharge curves can be normalized to the mass of the active material or the area of the electrode. In HC half-cells (as well as for LIBs), GCD results are generally represented as potential in the y-axis and gravimetric capacity (mAh g^{-1}) in the x-axis. The resulting U-shape curves (see Fig. 7b) consist of a slope region and a low-potential plateau, determined by the different Na^+ storage mechanism contribution. Once the half-cell is assembled, a negative current is applied between the WE and the CE (green arrow), resulting in the HC sodiation (point 1). When the cut-off potential is achieved (near 0 V), a positive current is applied, and the electrode desodiation takes place (red arrow). Charge and discharge capacities for each cycle can be obtained from the corresponding *x*-axis value when the process finishes. It should be noted that the capacity loss during the first cycle (orange lines) between the discharge (sodiation) and charge (de-sodiation) can be significant. This is due to the irreversible Na^+ trapping into the SEI and HC defects as well as other side reactions. The capacity loss during the first cycle is quantified by the ICE (Eq. (8)). By contrast, relatively similar discharge and charge capacities for the second and third cycles reveal a high reversible capacity.

$$\mathrm{ICE} = \left[\left(C_{\mathrm{discharge}_{(n_1)}} - C_{\mathrm{charge}_{(n_1)}}\right)/C_{\mathrm{discharge}_{(n_1)}}\right] \times 100\% \tag{8}$$

$$Q_{\mathrm{ret}} = \left[C_{\mathrm{discharge}_{(n)}}/C_{\mathrm{discharge}_{(n+1)}}\right] \times 100\% \tag{9}$$

The stability of the half-cell can be determined by consecutive charging/discharging cycles as shown in Fig. 7(c). The specific capacity, after falling for the first few *n* cycles, tends to stabilize and ideally slowly decrease for the successive rounds. The capacity retention (Q_{ret}, calculated using Eq. (9)) determines the lifespan of a battery, which is a key factor for its commercialization. Also of paramount importance is to know the behavior of the (half-)cell when is cycled at higher current intensities. In a rate capability assay (see Fig. 7d), the applied current is changed from lower to higher C rates; as a result, the specific capacity decreases, to a greater or lesser extent, depending on the HC conductivity, ion-diffusion distance, and Na^+ transport kinetics [311,312]. Finally, the cell is cycled again at the initial current rate to determine the possible retention capacity loss during the cycling at higher C rates.

In addition, Galvanostatic intermittent titration (GITT), which was proposed by Weppner and Huggins in 1977 [313], is a commonly used technique to estimate the apparent Na^+ diffusion coefficient (*D*). However, several assumptions have to be made for this purpose [314]: (i) dense planar electrode, (ii) constant and uniform current, (iii) one-dimensional diffusion, (iv) volume and structure electrode changes are not considered, (v) during each current pulse *D* can be considered constant, (vi) Fick's law of diffusion applies, and (vii) other no diffusional potential effects can be dismissed. The procedure comprises a series of current pulses, each followed by an open circuit voltage (OCV) rest period in which the electrode tends to the equilibrium state thanks to the Na ions diffusion. This sequence of constant current pulses and relaxation periods is repeated until the battery is fully sodiated or desodiated (see Fig. 7e). Since the diffusion coefficient is calculated for each pulse step, this technique allows plotting D values fluctuation along the sodiation and desodiation processes, which can help to identify the different Na^+ storage mechanisms occurring along the voltage window [315].

Under the above-listed assumptions, the apparent diffusion coefficient (*D*) can be estimated from Eq. (10), which derives from the Fick's second law of diffusion, where τ is the pulse time and m_B, V_M, M_B, *S* and *L* the mass, molar volume, molecular weight, electrochemical active area, and thickness of the electrode material, respectively. ΔE_s is the voltage variation in the rest state (without current circulation) and ΔE_τ is the transient voltage change when applying a galvanostatic current during the pulse. Both values for each current step can be obtained from the GITT curve, as shown in Fig. 7(f). It has to be highlighted that ($m_B V_M/M_B$) represents the volume of the electrode material [316] and also that *A* is not the surface area of the pristine hard carbon since, in the electrode, it is commonly attached to the binder and conductive additives [301]. To ease calculations, the electrode volume is assumed to be constant during the process and due to the simple geometry of a thin film electrode ($V = S{\cdot}L$), *D* can be estimated by Eq. (11). The pulse time must be short enough to ensure a linear relationship between E_τ and τ. Common τ values are between 10 and 30 min, followed by a relaxation period in the range of 1–2 h [172–174,311,317,318].

$$D = \frac{4}{\pi\tau}\left(\frac{m_B V_M}{M_B S}\right)^2\left(\frac{\Delta E_S}{\Delta E_\tau}\right)^2 (\tau \ll L^2/D) \tag{10}$$

$$D = \frac{4L^2}{\pi\tau}\left(\frac{\Delta E_S}{\Delta E_\tau}\right)^2 (\tau \ll L^2/D) \tag{11}$$

5.4. Impedance-based techniques

Impedance (*Z*) is defined as the opposition that the electrochemical system presents to an alternating current flow. A high cell impedance can produce large overpotentials, low energy efficiency, low rate capability, and even facilitate a thermal runaway [281]. Electrochemical Impedance Spectroscopy (EIS) is a widely used technique to estimate the impedance, kinetic, and diffusion parameters of the electrode processes. In EIS, a small perturbation in the form of an alternating signal of small magnitude is applied to the system to follow the signal at a steady state. EIS is normally conducted by applying an AC potential to the cell, thus the potential is modulated sinusoidally and then the cell current and its phase are measured. Since the technique is based on a linear response theory, imposed perturbations need to be small enough to maintain the electrochemical system under equilibrium. In the battery field, low amplitude of 1–10 mV vs. OCV and frequency ranges from 10^{-2} to 10^5 Hz are usually applied [301].

EIS can be extremely helpful to extract information on the different phenomena taking place in the cell, since each interphase process will contribute to the conduction of electrical current, to a greater or lesser extent, depending on its frequency [26]. The resulting electrochemical impedance spectra are usually represented by the Nyquist plot, where the data from each frequency point is plotted by the real (*Z'*) and the imaginary (*Z''*) parts of the impedance in the horizontal and vertical axis, respectively. Interpretation of EIS data is done by fitting the obtained curve to an equivalent electrical circuit (EEC) containing resistors, capacitors, and inductors.

The Nyquist plot usually consists of a single semicircle in the medium/high frequencies and a straight line in the low-frequency region. The former is associated with charge-transfer processes impedance and the double layer capacitance, while the straight line is related to the Na^+ diffusion into the bulk of the electrode material [319]. Fig. 7(g) shows a Nyquist plot together with the most used equivalent circuit, the *Randles equivalent circuit* [320–327], where R_e is the electrolyte resistance, R_{ct} is the interfacial charge transfer resistance (for the faradaic reactions at the electrode surface), C_{dl} is the electrical double layer capacitance, and *W* is the Warbug impedance associated with Na^+ diffusion into the electrode [190,324]. From the Nyquist plot, resistances can be

obtained from the horizontal axis, while capacitive impedances have a vertical component.

A second approach arises from the presence of two semicircles in the Nyquist plot, more or less overlapped once the cell is cycled [328]. This new semicircle located in the high frequencies is attributed to the SEI formation and, consequently, a new parallel combination of a resistor and a capacitor is added to the equivalent circuit (see Fig. 7h) [329–338], where R_{SEI} is the resistance associated with the SEI film and C_{SEI} the capacitance related to the passivation layer. EIS is also used to determine diffusion kinetics during sodium ion intercalation/deintercalation processes, since as discussed above, the Warburg impedance is related to the ion diffusion [339,340]. The EIS-derived diffusion coefficient can be calculated from Eq. (12), where R is the gas constant, T is the ambient temperature, A is the surface area of the electrode, F is the Faraday constant, C is the Na^+ concentration in the electrode, n is the number of electrons per charge carrier (n = 1 for Na^+), and σ is the Warburg coefficient obtained from the slope of the fitted line Z' vs. $\omega^{-1/2}$, being ω the angular frequency.

$$D = \frac{R^2T^2}{2A^2F^4\sigma^2C^2n^4} \tag{12}$$

The third and more sophisticated equivalent circuit type is that based on the Transmission Line Model (TLM) for porous electrodes [341]. TLM models for cylindrical pores were developed and applied to characterize positive and negative electrodes in LIBs [342–346]. Landesfeind [347] and Pritzl [348] proposed a TLM-based equivalent circuit (represented in Fig. 7i) to analyze the impedance spectra of LIB cathodes and anodes. This equivalent circuit was divided in four sections for a graphitic anode: (i) The high frequency resistance (R_{HFR}), which comprises the ionic resistance of the separator and the external electronic cell contacts resistance; (ii) the ionic contact resistance of a thin layer in the graphite surface adjacent to the separator; (iii) the impedance associated with the ion and electron conduction through the porous anode, described by the TLM and composed of differential elements: charge transfer resistance (r_{CT}), double layer capacitance (q_{CT}), pure ionic resistance (r_{Pore}), and electrical resistance ($r_{El.}$); and, (iv) the Warbug diffusion element (W) at low frequencies reflecting liquid concentration gradients inside the separator. It should be pointed out that constant phase elements (Q) are used to model the behavior of the double layer [349]. The same equivalent circuit was also used by Linsenmann et al. [170,171] for in-situ impedance measurements of a hard carbon anode in a SIB.

5.5. Two vs. three electrode setup

Two-electrode half-cell configuration (using either coin- or Swagelok-type cells) is the widely used setup when electrodes are studied in the context of Li and Na chemistries. The electrode of interest is assigned as the WE, while the other serves as both the CE and RE. However, despite the experimental simplicity and easy construction, the use of the two-electrode hardware needs to be delimited. Two-electrode setup can be suitable to measure the behavior of the tested material at relatively low current densities for comparison purposes. In contrast, three-electrode setups (see Fig. 8) are a priori desirable to separate the contributions of WE and CE, since the insertion of a third electrode (RE) allows the simultaneous potential or impedance acquisition of both WE and CE during testing.

When a given active material is characterized using a 2-electrode cell, it is assumed that the electrochemical response at the CE is negligible and, therefore, the measured overall result represents the properties of the active material under study. As shown in Section 2.6, to be a good RE in addition to a CE, the corresponding material should have a small overpotential and a stable voltage during all the measurement time. In the case of LIBs, the voltage of a lithium metal electrode is only reproducible at current densities lower than 1 mA cm^{-2} due to dendrites formation [199]. Undervalued rate capability during GCD and EIS misinterpretations are potential two-electrode-derived drawbacks. Further details on both phenomena are provided in the next subsections.

5.5.1. Undervalued rate capability

Costard et al. [208] revealed how metallic lithium CEs introduced additional overpotentials in two-electrode setups, which led to the underestimation of the anode rate capability. Hence, they strongly recommended the use of a three-electrode setup for GCD experiments. In the same line, Li et al. [350] measured the rate capability of HC-based anodes for SIBs by cycling them in two and three-electrode half-cell setups. At a current rate of 250 mA g^{-1}, when the three-electrode cell was used, the HC anode delivered a capacity of 186 mAh g^{-1}; however, when the two-electrode setup was employed, only a capacity of 118 mAh g^{-1} was measured.

Metallic sodium CE polarization is due to the formation of a passivation layer on its surface during discharge. This layer is subsequently dissolved during the subsequent charging step [351]. Therefore, in a half-cell, the Na RE/CE suffers from the resulting

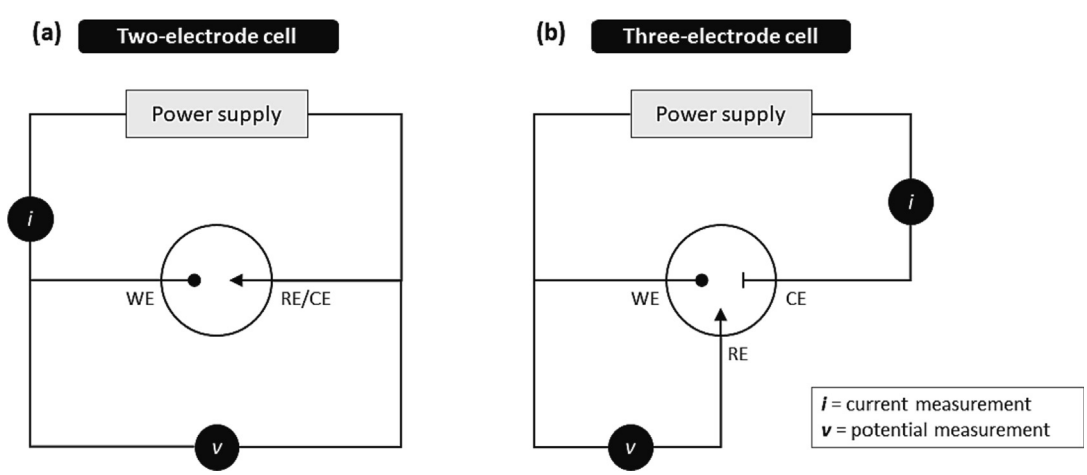

Fig. 8. Cell setup with (a) two electrode and (b) three electrode configurations.

ohmic resistance and the consequent overpotential. Any extent of overpotential at the sodium metal electrode, particularly at high rates, drives the half-cells to reach the lower cutoff potential prematurely, hindering the full sodiation of the HC anode. Fig. 9 shows how part of the HC sodiation potential is below that of the CE, and therefore the capacity of this segment is not counted in half-cells. Since a considerable part of the sodiation is available in the low-potential plateau region (<0.1 V vs. Na/Na^+), two-electrode setups may give rise to major errors in the anode capacity measurement, especially at higher C rates.

Zheng et al. [190] also found this capacity fading problem in SIB half-cells cycled at high rates. They suggested the use of full-cell setups to check the rate capability of HC-based electrodes using a sodium transition metal oxide as cathode. In another article [352], the same authors also proposed a new method to avoid capacity underestimation in half-cells by sodiating the HC until slightly-negative voltages. However, Na metal plating and dendritic growth on the HC surface can certainly take place after exceeding a certain negative voltage, as stated in Section 5.3. This phenomenon is known to be irreversible and to form "dead Na" and liquid electrolyte dryout. However, the authors also found that a V-shaped peak on the voltage profile appeared before the undesirable plating occurs, allowing the establishment of a safe cut-off voltage.

5.5.2. EIS misinterpretations

The use of two- or three-electrode cells is also a determinant for accurate measurement of the electrochemical impedance spectra. EIS of two-electrode cells can be obtained easily, but it represents the sum of the impedance of both electrodes (WE and CE). Several interfacial diffusional processes (charge transfer) take place in both electrodes and the resulting semicircles may overlapped in the same range of frequency, leading to misinterpretation. Moreover, the impedance of the metallic CE is larger than that of a porous HC electrode [201,353]. In order to obtain a reliable impedance spectrum of a single electrode, using a symmetric cell or a three-electrode setup is suggested.

Symmetric cells are made up of two identical electrodes and allow the obtention of the anode impedance by dividing by two the measured one [354,355]. However, this configuration only enables the characterization of uncycled electrodes. To study the impedance evolution of an electrode during charge and discharge cycles, it would be necessary to disassemble the battery and extract the electrode for each measurement. It would be a delicate and laborious process that would reduce the representativity and reproducibility of the real electrochemical behavior inside the battery [356].

Three-electrode setup allows the WE impedance to be monitored with respect to a RE, regardless of the CE. For this purpose, the most commonly used system is the three-electrode Swagelok T-cell with a point-like RE geometry. Under this system (see Fig. 5c), a metal disc (Na in SIBs) is placed in contact with the separator at the edge of the WE and CE, outside the active area [213,287,357,358]. However, this configuration was proven to be unreliable for EIS. Imprecise electrode alignment and asymmetric RE geometry cause EIS distortions such as scaling, inductive or even artificial capacitive loops in the spectra.

Ender et al. [359] found two fundamental effects that cause distortions and artifacts in three-electrode LIB half-cell impedance spectra: geometrical and electrochemical asymmetry. Both result in a frequency dependent variation of ionic current line distributions. Ender and coworkers investigated three different RE geometries by finite element method (FEM) simulations: point-like, wire, and mesh REs. The first geometry showed strong impacts and caused large artifacts, while the other two geometries exhibited considerably lower or even negligible artifacts. Klink et al. [286,360] and Bünzli et al. [353] used lithium metal micro reference electrodes placed at the center of working and counter ring electrodes in a coaxial position. However, although these systems can reduce artifacts, their construction is complex and impedance response is still highly sensitive in terms of electrode alignment [361].

In view of the current state of knowledge, the following recommendations should be considered in order to avoid the above-described artifacts: (i) minimizing the geometric asymmetry: CE and WE should be of the same size and perfectly aligned [208]; (ii) since the presence of the RE hinders the transport of ions in the electrolyte, a small size RE is required to minimize the transport resistance between the WE and CE [362]; and (iii) to prevent distortions, the best RE location is between the WE and the CE, where the electric field is homogeneous [204,363].

Coin-type cells were already modified to insert a micro-reference electrode sandwiched between the WE and CE [137,200,209,364]. However, to connect the RE, a small hole must be made in the cell and sealed with an epoxy resin. As a result, these cells are difficult to build and have a high failure rate. Moreover, they are not compatible with volatile solvents since an increase in internal pressure can cause leaks through the epoxy resin [22]. On the other hand, micro-reference wire electrodes placed between the WE and CE electrodes may be appropriate for LIBs. The wire needs to be insulated (e.g., using polyurethane) in order to keep access to the electrolyte only the cut cross-section at the tip of the wire. In this way, side reactions are minimized and a long-term stable potential in the RE can be reached. Once placed centrally inside the cell, between two separators, the metallic wire is in-situ electrochemically alloyed with lithium (lithiated) to obtain a stable reference potential. Zhou et al. [365] followed this procedure using a 40-μm-diameter copper wire,

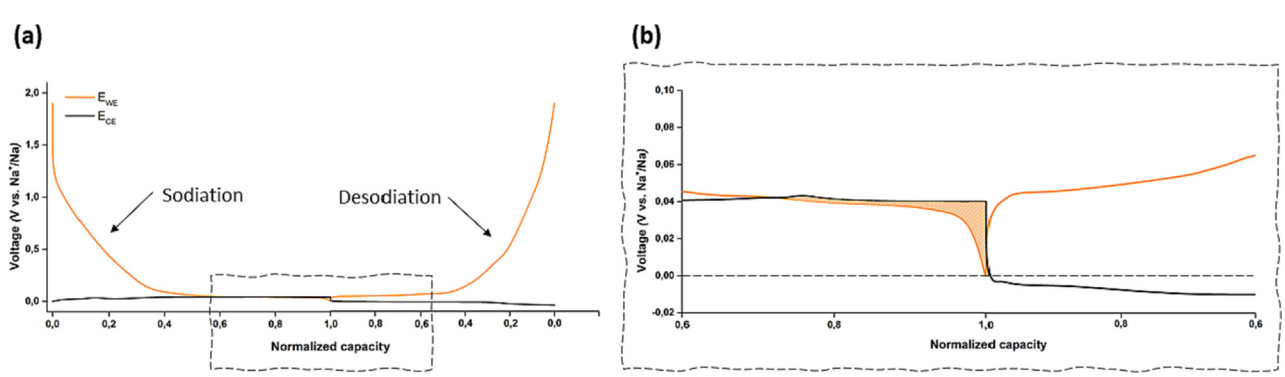

Fig. 9. Expected sodiation–desodiation potential profiles of hard carbon in three-electrode cells. E_{we} (orange) and E_{ce} (black) vs. normalized capacity are plotted in the full sodiation–desodiation range (a) and the zoomed equivalent (b). Reproduced from Ref. [350] with permission from Royal Society of Chemistry.

whereas Abraham et al. [200] and Jansen et al. [203] used a 25-μm-diameter tin-coated copper wire. Solchenbach et al. [30] designed a 50 μm thick lithium-gold micro-reference electrode, resulting stable for more than 500 h and allowing impedance measurements in LFP/graphite full-cells for up to 200 cycles.

A micro-RE was designed for SIBs by Linsenmann et al. [170], who used a 50 μm-sized tin-coated copper wire (μ-TWRE) insulated with a polyurethane spray. The μ-TWRE was subject to an in situ galvanostatic sodiation by applying a charging current of 50 nA until a potential cutoff of 10 mV vs. Na/Na^+ was reached. However, when a high-impedance μ-RE (e.g., μ-TWRE) is used, resistances of WE and CE have to be in the same order of magnitude to obtain reliable single-electrode EIS data [366]. Since metallic sodium has a much higher impedance than that of hard carbon, Linsenmann et al. attached a high-surface area carbon fiber paper on the metallic sodium electrode face, lowering its impedance thanks to chemical interactions between both materials [366]. This setup allowed the authors to obtain the impedance evolution of an HC anode during 50 charge/discharge cycles in a half-cell SIB. It must be highlighted, however, that this setup allows the HC EIS measurement, but unfortunately the sodiated μ-TWRE is not stable enough to be used as RE during cyclic GCD measurements.

6. Carbon characterization techniques

Hard carbons must be characterized in order to link their physicochemical properties with the electrochemical performance of the electrode. The main techniques used for this purpose are outlined below.

X-ray diffraction (XRD) is a non-destructive analytical technique used to determine the material crystalline phases. Fig. 10 (a) shows the typical XRD pattern of an amorphous carbon with graphitic domains, in which two peaks appear around 23° and 43°. The former is ascribed to the (002) crystal plane of graphitic sheets and the second one to the (100) plane of sp^2-hybridized hexagonal carbons [139]. The interlayer space between graphene layers (d_{002}) can be calculated by the Bragg equation (Eq. (13)) from the (002) plane values, where λ is the wavelength of the X-rays and θ is the angle of the peak (in degrees).

$$d = \frac{\lambda}{2\sin\theta} \tag{13}$$

$$L = \frac{K\lambda}{\beta\cos\theta} \tag{14}$$

$$n = \frac{L_c}{d_{002}} \tag{15}$$

The apparent crystallite thickness along the c-axis (L_c) and the apparent crystallite width along the a-axis (L_a) (see Fig. 10b) can be obtained from the Scherrer's formula in Eq. (14) and the (002) and (100) planes, respectively. As shown in Fig. 10(a), β is the full width at half-maximum (FWHM) of the XRD peaks (in radians) [367]; K is the form or shape factor, with common values of 1.84 for L_a and 0.9 for L_c [368–370]. In addition, the number of graphene stacking layers (n) can be estimated from Eq. (15) [330].

Ex situ XRD analysis of cycled anodes at different voltages can be used to obtain information about their structural evolution during sodiation and desodiation processes [311]. Cell modifications may also be done to allow in situ XRD analysis during cycling [371].

Raman spectroscopy is another widely used technique to investigate the nanoscale structure and the disorder degree of carbon-based materials [372,373]. Raman spectra of hard carbon usually show two characteristic peaks around 1350 cm^{-1} (D band) and 1600 cm^{-1} (G band), as shown in Fig. 10(c). The G band is associated with the crystalline graphite carbon, while the D band refers to lattice defects and amorphous carbon [374,375]. The intensity ratio (I_D/I_G) is commonly used to quantify the degree of structural disorder. To quantify I_D/I_G, the ideal procedure involves the preliminary deconvolution of the Raman spectra into one Gaussian-shaped band (D3) and four Lorentzian-shaped bands (G, D1, D2, and D4) [376]; then, the peak area ratio (A_{D1}/A_G) can be calculated as the I_D/I_G ratio (see Fig. 10c).

Raman spectra can also be used to obtain L_a via Eq. (16) [377], where λ_l is the laser line wavelength (in nm). Finally, ex-situ [378] and in-situ [379] Raman spectroscopy of cycled electrodes also allow investigating the sodium storage mechanism into hard carbon and the influence on the electrode structure.

$$L_a = (2.4 \times 10^{-10})\lambda_l^4 \left(\frac{I_D}{I_G}\right)^{-1} \tag{16}$$

Gas sorption porosimetry techniques are required to estimate the surface area and pore size distribution of HC materials. N_2 adsorption–desorption isotherms at 77 K are commonly carried out to calculate the Brunauer–Emmett–Teller (BET) surface area, often related to the magnitude of the SEI, and also to obtain the micropore volume assuming the non-local density functional theory (NLDFT) [380]. However, nitrogen cannot properly access to pores smaller than 0.7 nm due to kinetic limitations and specific interactions with surface functional groups. Moreover, N_2 suffers from restricted diffusion into the narrowest micropores of width minor than 0.45 nm [381]. Therefore, N_2 sorption porosimetry may underestimate the pore accessibility for electrolyte molecules. On the other hand, CO_2 isotherms at 273.15 K have been suggested to calculate the BET surface area of materials containing very small pores (i.e., ultra-micropores) [382,383]. Lastly, hard carbon macroporosity can be determined by mercury intrusion [384].

Electron microscopy is commonly used to investigate the morphology of hard carbons. Scanning electron microscopy (SEM) allows to determine particle size distributions and pore morphologies. For a more detailed morphological characterization, high resolution transmission electron microscopy (HR-TEM) provides access to much information about the sample, such as analyzing the microcrystalline structure and allowing the identification of pseudographitic domains, defects and nanovoids [140,192]. Thus,

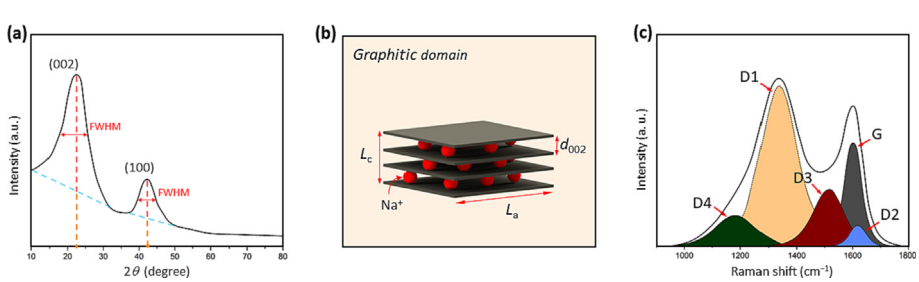

Fig. 10. (a) XRD typical pattern for HCs, (b) apparent graphitic domain distances, and (c) Raman spectra deconvolution.

HR-TEM images are helpful in determining the carbon ordering degree and even the interlayer spacing [325]. Complementary, the selected area electron diffraction (SAED) patterns of turbostratic carbons show the two dispersed diffraction rings associated with the (0 0 2) and (1 0 0) planes [169] and also indicate the ordering degree. The sharper the diffraction rings, the higher the carbon graphitization degree [315,385].

Chemical composition of HCs is also a determining factor for its performance as anode. Energy-dispersive X-ray spectroscopy (EDS) allows the elemental composition to be measured, and, together with SEM [386] or TEM [387], provides element mapping images. The latter is widely employed when HC is doped to check if heteroatoms (N, P, S, etc.) are uniformly distributed. In addition, X-ray photoelectron spectroscopy (XPS) is the other prevailed composition technique and is conducted to study surface chemical bonding. The XPS spectrum of the C 1*s* region provides the percentages of C—C bond (defect-free graphite lattice) and the C—O and C=O bonds (defective graphite lattice). In parallel, oxygen containing functional groups C=O and C—OH can be obtained from the XPS spectra in the O 1*s* region [335]. Moreover, the chemical state of heteroatoms in doped HCs can be obtained from the specific regions of the XPS spectra (e.g., N 1*s*, S 2*p*, and P 2*p*) [388].

Beyond the above-mentioned most popular techniques and procedures, there are additional analytical techniques that can provide valuable insights. For instance, small angle X-ray scattering (SAXS) is employed to detect both open and closed pores [389], while X-ray fluorescence (XRF) allows to determinate the concentration of inorganic elements in the hard carbon [390]. X-ray total scattering and pair distribution function analysis (PDF) [391] can also be used to observe changes in the local structure and determine the interplane and in-plane interatomic distances. Finally, nuclear magnetic resonance (NMR) spectroscopy [296,392] is available to assess the carbon chemical composition and also to determine the different electronic and local structures of the Na inserted during cycling.

7. Conclusions and prospects

Sodium-ion batteries are one of the most promising candidates to replace LIBs in energy storage applications. In this context, numerous studies are being carried out to improve this technology, particularly with regard to the anodes. In this review, we have tried to provide the basic guidelines required to characterize new carbonaceous electrodes. First of all, a proper selection of both the cell setup and the electrochemical techniques is crucial for an accurate characterization of the anodes. In this regard, standardized procedures would facilitate the comparison of performance indicators to move research in the right direction.

This article focuses on the use of half-cell batteries as they have proven to be effective and because they are the most widely used. However, it should not be forgotten that the next step should be the characterization of these carbonaceous anodes in full-cells using commercially available cathodes. The utilization of coin half-cells seems suitable for comparing the electrochemical performance of a series of carbons at the intra-study level. Both the parts and the necessary equipment are commercially distributed and multichannel coin cell testing boards are available for quick characterization. However, more studies are required to determine the probable rate capability undervaluation as well as other alternative 3-electrode setups to perform EIS measurements. It should also be noted the importance of reporting the GCD applied current intensity when comparing the capacity of an electrode with the literature, since linking capacities obtained at different specific intensities is not consistent because of the known diffusional limitations of carbon electrodes.

Regarding the device materials, PEEK and polyolefins seem to be the best insulators for SIBs, while laboratory fiberglass filters can be chosen as inexpensive separators. As a current collector, the aluminum foil should be systematically used in both electrodes since it does not alloy with sodium, in contrast to LIBs. A change from PVDF/NMP to water-soluble binders (CMC, SBR, PAA, and Na-Alg) should also be adopted since they provide better electrochemical performances besides being low-cost and environmentally benign.

Research into better electrolytic systems is also essential to enable advanced and viable SIBs. Ester-derived electrolytes are the most studied; therefore, determining hard carbon performance in those electrolytes allows comparing results with a broad number of published articles. We recommend the use of fluorinated salts, such as $NaPF_6$ or NaTFSI, as well as studying the use of additives to improve half-cell results. Ether-based are the second most explored electrolytes and they are becoming increasingly attractive to be used in SIBs based on HCs anodes. The composition of SEI layers on HC electrodes is strongly affected by electrolyte changes, thus, exploring novel electrolytes is a key factor for the future of SIBs.

Finally, a guideline with basic electrochemical concepts, the most widely used techniques (CV, GCD, GITT, and EIS), and some basic carbon characterization techniques (XRD, Raman, etc.) were provided. We hope that the herein collected theorical foundations explained from a practical point of view provide new researchers with an accessible and comprehensive guide to systematically improve the electrochemical performance of carbonaceous materials.

Declaration of competing interest

The authors declare that they have no known competing financial interests or personal relationships that could have appeared to influence the work reported in this paper.

Acknowledgments

This work is part of the research project PID2019-107737RB-I00, funded by MCIN/AEI/10.13039/501100011033. The authors also acknowledge the funding from the Aragón Government (Ref. T22_20R), funded by FEDER 2014-2020 "Construyendo Europa desde Aragón". DA also acknowledges the funding from the Regional Government of Aragon (Spain) with a grant for postgraduate research contracts (2019-2023).

References

[1] European Commission, Critical Raw Materials Resilience: Charting a Path towards Greater Security and Sustainability, Brussels, 2020.
[2] R.S. Carmichael, Practical Handbook of Physical Properties of Rocks and Minerals (1988), CRC Press, 2017.
[3] N.N. Greenwood, A. Earnshaw, in: Chem. Elem., Second Edi, Elsevier, 1997, pp. 68–106.
[4] T.E. Fan, H.F. Xie, J. Alloys Compd. 775 (2019) 549–553.
[5] J. Barker, C.J. Wright, Storage and/or Transport of Sodium-Ion Cells, WO 2016/027082 Al, 2016.
[6] C. Fear, D. Juarez-Robles, J.A. Jeevarajan, P.P. Mukherjee, J. Electrochem. Soc. 165 (2018) A1639–A1647.
[7] M. Okoshi, Y. Yamada, A. Yamada, H. Nakai, J. Electrochem. Soc. 160 (2013) A2160–A2165.
[8] P.K. Nayak, L. Yang, W. Brehm, P. Adelhelm, Angew. Chem. – Int. Ed. 57 (2018) 102–120.
[9] Y. Sun, S. Guo, H. Zhou, Energy Environ. Sci. 12 (2019) 825–840.
[10] A. Bauer, J. Song, S. Vail, W. Pan, J. Barker, Y. Lu, Adv. Energy Mater. 8 (2018) 1–13.
[11] S. Komaba, W. Murata, T. Ishikawa, N. Yabuuchi, T. Ozeki, T. Nakayama, A. Ogata, K. Gotoh, K. Fujiwara, Adv. Funct. Mater. 21 (2011) 3859–3867.
[12] D. Linden, T.B. Reddy, Handbook of Batteries, Third edit, McGraw-Hill, New York, Chicago, San Francisco, Lisbon, London, Madrid, Mexico City, Milan, New Delhi, San Juan, Seoul, Singapore, Sydney, Toronto, 2002.

[13] A.J. Bard, G. Inzelt, F. Scholz, Electrochemical Dictionary, Springer-Verlag, Berlin Heidelberg, 2008.
[14] N.N. Sinha, J.C. Burns, R.J. Sanderson, J. Dahn, J. Electrochem. Soc. 158 (2011) A1400.
[15] A.S. Baranski, W.R. Fawcett, J. Electrochem. Soc. 129 (1982) 901–907.
[16] Y. Hamon, T. Brousse, F. Jousse, P. Topart, P. Buvat, D.M. Schleich, J. Power Sources 97–98 (2001) 185–187.
[17] J.Y. Hwang, S.T. Myung, Y.K. Sun, Chem. Soc. Rev. 46 (2017) 3529–3614.
[18] A. Bhide, J. Hofmann, A. Katharina Dürr, J. Janek, P. Adelhelm, Phys. Chem. Chem. Phys. 16 (2014) 1987–1998.
[19] A. Ponrouch, E. Marchante, M. Courty, J.M. Tarascon, M.R. Palacín, Energy Environ. Sci. 5 (2012) 8572–8583.
[20] L. Lutz, D. Alves Dalla Corte, M. Tang, E. Salager, M. Deschamps, A. Grimaud, L. Johnson, P.G. Bruce, J.M. Tarascon, Chem. Mater. 29 (2017) 6066–6075.
[21] H.S. Lim, J.D. Margerum, S.A. Verzwyvelt, A.M. Lackner, R.C. Knechtli, J. Electrochem. Soc. 136 (1989) 605–612.
[22] K. Periyapperuma, T.T. Tran, S. Trussler, D. Ioboni, M.N. Obrovac, J. Electrochem. Soc. 161 (2014) A2182–A2187.
[23] S. Tasker, R.D. Chambers, J.P.S. Badyal, J. Phys. Chem. 98 (1994) 12442–12446.
[24] L. Guobao, X. Rongjian, L. Chen, Solid State Ionics 90 (1996) 221–225.
[25] K. Westman, R. Dugas, P. Jankowski, W. Wieczorek, G. Gachot, M. Morcrette, E. Irisarri, A. Ponrouch, M.R. Palacín, J.M. Tarascon, P. Johansson, ACS Appl. Energy Mater. 1 (2018) 2671–2680.
[26] R. Dugas, J.D. Forero-Saboya, A. Ponrouch, Chem. Mater. 31 (2019) 8613–8628.
[27] G. Garcia, W. Schuhmann, E. Ventosa, ChemElectroChem 3 (2016) 592–597.
[28] K. Pfeifer, S. Arnold, J. Becherer, C. Das, J. Maibach, H. Ehrenberg, S. Dsoke, ChemSusChem 12 (2019) 3312–3319.
[29] A.A. Heidari, H. Mahdavi, Chem. Rec. 20 (2020) 570–595.
[30] S. Solchenbach, D. Pritzl, E.J.Y. Kong, J. Landesfeind, H.A. Gasteiger, J. Electrochem. Soc. 163 (2016) A2265–A2272.
[31] T.C. Nirmale, B.B. Kale, A.J. Varma, Int. J. Biol. Macromol. 103 (2017) 1032–1043.
[32] J. Zhu, M. Yanilmaz, K. Fu, C. Chen, Y. Lu, Y. Ge, D. Kim, X. Zhang, J. Memb. Sci. 504 (2016) 89–96.
[33] X. Luo, W. Pan, H. Liu, J. Gong, H. Wu, Ionics (Kiel). 21 (2015) 3135–3139.
[34] R. Arunkumar, A.P. Vijaya Kumar Saroja, R. Sundara, ACS Appl. Mater Interfaces 11 (2019) 3889–3896.
[35] J.H. Jo, C.H. Jo, Z. Qiu, H. Yashiro, L. Shi, Z. Wang, S. Yuan, S.T. Myung, Front. Chem. 8 (2020) 1–12.
[36] Y. Cao, L. Xiao, M.L. Sushko, W. Wang, B. Schwenzer, J. Xiao, Z. Nie, L.V. Saraf, Z. Yang, J. Liu, Nano Lett. 12 (2012) 3783–3787.
[37] X. Xia, J.R. Dahn, Electrochem. Solid-State Lett. 15 (2012) 2–6.
[38] M. D'Arienzo, R. Ruffo, R. Scotti, F. Morazzoni, C.M. Mari, S. Polizzi, Phys. Chem. Chem. Phys. 14 (2012) 5945–5952.
[39] R. Berthelot, D. Carlier, C. Delmas, Nat. Mater. 10 (2011) 74–80.
[40] R. Alcántara, J.M. Jiménez-Mateos, P. Lavela, J.L. Tirado, Electrochem. Commun. 3 (2001) 639–642.
[41] Y. Cao, L. Xiao, W. Wang, D. Choi, Z. Nie, J. Yu, L.V. Saraf, Z. Yang, J. Liu, Adv. Mater. 23 (2011) 3155–3160.
[42] Y. Xiao, P.F. Wang, Y.X. Yin, Y.F. Zhu, X. Yang, X.D. Zhang, Y. Wang, X.D. Guo, B. H. Zhong, Y.G. Guo, Adv. Energy Mater. 8 (2018) 1–7.
[43] H. Wang, X.-Z. Liao, Y. Yang, X. Yan, Y.-S. He, Z.-F. Ma, J. Electrochem. Soc. 163 (2016) A565–A570.
[44] N. Yabuuchi, M. Kajiyama, J. Iwatate, H. Nishikawa, S. Hitomi, R. Okuyama, R. Usui, Y. Yamada, S. Komaba, Nat. Mater. 11 (2012) 512–517.
[45] R. Dugas, B. Zhang, P. Rozier, J.M. Tarascon, J. Electrochem. Soc. 163 (2016) A867–A874.
[46] D. Buchholz, A. Moretti, R. Kloepsch, S. Nowak, V. Siozios, M. Winter, S. Passerini, Chem. Mater. 25 (2013) 142–148.
[47] M. Sathiya, K. Hemalatha, K. Ramesha, J.M. Tarascon, A.S. Prakash, Chem. Mater. 24 (2012) 1846–1853.
[48] S. Komaba, T. Ishikawa, N. Yabuuchi, W. Murata, A. Ito, Y. Ohsawa, ACS Appl. Mater. Interfaces 3 (2011) 4165–4168.
[49] M. Dahbi, M. Kiso, K. Kubota, T. Horiba, T. Chafik, K. Hida, T. Matsuyama, S. Komaba, J. Mater. Chem. A 5 (2017) 9917–9928.
[50] S.M. Oh, S.T. Myung, C.S. Yoon, J. Lu, J. Hassoun, B. Scrosati, K. Amine, Y.K. Sun, Nano Lett. 14 (2014) 1620–1626.
[51] Z. Zeng, X. Jiang, R. Li, D. Yuan, X. Ai, H. Yang, Y. Cao, Adv. Sci. 3 (2016) 1–8.
[52] Y. Yu, H. Che, X. Yang, Y. Deng, L. Li, Z.F. Ma, Electrochem. Commun. 110 (2020) 106635.
[53] Y. Zhu, Y. Xu, Y. Liu, C. Luo, C. Wang, Nanoscale 5 (2013) 780–787.
[54] P. Moreau, D. Guyomard, J. Gaubicher, F. Boucher, Chem. Mater. 22 (2010) 4126–4128.
[55] D.R. Kumar, I. Kanagaraj, G. Dhakal, A.S. Prakash, J.J. Shim, J. Environ. Chem. Eng. 9 (2021) 105698.
[56] M.K. Sadan, H. Kim, C. Kim, S.H. Cha, K.K. Cho, K.W. Kim, J.H. Ahn, H.J. Ahn, J. Mater. Chem. A 8 (2020) 9843–9849.
[57] L.L. Driscoll, E. Kendrick, K.S. Knight, A.J. Wright, P.R. Slater, J. Solid State Chem. 258 (2018) 64–71.
[58] N. Recham, J.-N. Chotard, L. Dupont, K. Djellab, M. Armand, J.-M. Tarascon, J. Electrochem. Soc. 156 (2009) A993.
[59] J. Barker, M.Y. Saidi, J.L. Swoyer, Electrochem. Solid-State Lett. 6 (2003) A1.
[60] H. Zhuo, X. Wang, A. Tang, Z. Liu, S. Gamboa, P.J. Sebastian, J. Power Sources 160 (2006) 698–703.
[61] C. Vidal-Abarca, P. Lavela, J.L. Tirado, A.V. Chadwick, M. Alfredsson, E. Kelder, J. Power Sources 197 (2012) 314–318.
[62] R. Dugas, A. Ponrouch, G. Gachot, R. David, M.R. Palacin, J.M. Tarascon, J. Electrochem. Soc. 163 (2016) A2333–A2339.
[63] P. Barpanda, J.N. Chotard, N. Recham, C. Delacourt, M. Ati, L. Dupont, M. Armand, J.M. Tarascon, Inorg. Chem. 49 (2010) 7401–7413.
[64] F. Bianchini, H. Fjellvåg, P. Vajeeston, Phys. Chem. Chem. Phys. 19 (2017) 14462–14470.
[65] C. Deng, S. Zhang, B. Zhao, Energy Storage Mater. 4 (2016) 71–78.
[66] Y. Lu, L. Wang, J. Cheng, J.B. Goodenough, Chem. Commun. 48 (2012) 6544–6546.
[67] J. Qian, C. Wu, Y. Cao, Z. Ma, Y. Huang, X. Ai, H. Yang, Adv. Energy Mater. 8 (2018) 1–24.
[68] M. Lee, J. Hong, J. Lopez, Y. Sun, D. Feng, K. Lim, W.C. Chueh, M.F. Toney, Y. Cui, Z. Bao, Nat. Energy 2 (2017) 861–868.
[69] H. Kim, J.E. Kwon, B. Lee, J. Hong, M. Lee, S.Y. Park, K. Kang, Chem. Mater. 27 (2015) 7258–7264.
[70] S. Wang, L. Wang, Z. Zhu, Z. Hu, Q. Zhao, J. Chen, Angew. Chemie 126 (2014) 6002–6006.
[71] J. Wu, G. Hu, K. Du, Z. Peng, M. Huang, J. Fan, Y. Gong, D. Guan, Y. Shi, R. Liu, Y. Cao, Electrochim. Acta 403 (2022) 139641.
[72] Y. Fang, X.-Y. Yu, X.W. Lou, Angew. Chem. Int. Ed. 56 (2017) 5801–5805.
[73] B. Fu, X. Zhou, Y. Wang, J. Power Sources 310 (2016) 102–108.
[74] Y. Bai, L. Zhao, C. Wu, H. Li, Y. Li, F. Wu, ACS Appl. Mater. Interfaces 8 (2016) 2857–2865.
[75] J. Hwang, J. Kim, T. Yu, Y. Sun, Adv. Energy Mater. 9 (2019) 1803346.
[76] W. Tang, X. Song, Y. Du, C. Peng, M. Lin, S. Xi, B. Tian, J. Zheng, Y. Wu, F. Pan, K. P. Loh, J. Mater. Chem. A 4 (2016) 4882–4892.
[77] Y. Fang, L. Xiao, X. Ai, Y. Cao, H. Yang, Adv. Mater. 27 (2015) 5895–5900.
[78] M.Y. Wang, J.Z. Guo, Z.W. Wang, Z.Y. Gu, X.J. Nie, X. Yang, X.L. Wu, Small 16 (2020) 1–10.
[79] Z. Gu, J. Guo, J. Cao, X. Wang, X. Zhao, X. Zheng, W. Li, Z. Sun, H. Liang, X. Wu, Adv. Mater. 34 (2022) 2110108.
[80] L. Wang, J. Song, R. Qiao, L.A. Wray, M.A. Hossain, Y.-D. Chuang, W. Yang, Y. Lu, D. Evans, J.-J. Lee, S. Vail, X. Zhao, M. Nishijima, S. Kakimoto, J.B. Goodenough, J. Am. Chem. Soc. 137 (2015) 2548–2554.
[81] H.-W. Lee, R.Y. Wang, M. Pasta, S. Woo Lee, N. Liu, Y. Cui, Nat. Commun. 5 (2014) 5280.
[82] X. Wu, C. Wu, C. Wei, L. Hu, J. Qian, Y. Cao, X. Ai, J. Wang, H. Yang, ACS Appl. Mater. Interfaces 8 (2016) 5393–5399.
[83] M. Xie, Y. Huang, M. Xu, R. Chen, X. Zhang, L. Li, F. Wu, J. Power Sources 302 (2016) 7–12.
[84] W. Zhou, X. Zhang, W. Zhang, W. Huang, B. Yan, H. Li, S. Yu, Org. Electron. 82 (2020) 105702.
[85] S.E. Lee, M.H. Tang, J. Electrochem. Soc. 166 (2019) A3260–A3264.
[86] D. Aurbach, E. Zinigrad, Y. Cohen, Teller, Solid State Ionics 148 (2002) 405–416.
[87] L. Raguette, R. Jorn, J. Phys. Chem. C 122 (2018) 3219–3232.
[88] K. Edström, T. Gustafsson, J.O. Thomas, Electrochim. Acta 50 (2004) 397–403.
[89] D.I. Iermakova, R. Dugas, M.R. Palacín, A. Ponrouch, J. Electrochem. Soc. 162 (2015) A7060–A7066.
[90] R. Mogensen, D. Brandell, R. Younesi, ACS Energy Lett. 1 (2016) 1173–1178.
[91] O. Lenchuk, P. Adelhelm, D. Mollenhauer, Phys. Chem. Chem. Phys. 21 (2019) 19378–19390.
[92] M. Jäckle, A. Groß, J. Chem. Phys. 141 (2014) 174710.
[93] H. Kang, Y. Liu, K. Cao, Y. Zhao, L. Jiao, Y. Wang, H. Yuan, J. Mater. Chem. A 3 (2015) 17899–17913.
[94] L.D. Ellis, T.D. Hatchard, M.N. Obrovac, J. Electrochem. Soc. 159 (2012) A1801–A1805.
[95] J.H. Choi, C. Lee, S. Cho, G.D. Moon, B. su kim, H. Chang, H.D. Jang, Carbon N. Y. 132 (2018) 16–24.
[96] M. Song, C. Wang, D. Du, F. Li, J. Chen, Sci. China Chem. 62 (2019) 616–621.
[97] M. Fukunishi, N. Yabuuchi, M. Dahbi, J.Y. Son, Y. Cui, H. Oji, S. Komaba, J. Phys. Chem. C 120 (2016) 15017–15026.
[98] S. Komaba, Y. Matsuura, T. Ishikawa, N. Yabuuchi, W. Murata, S. Kuze, Electrochem. Commun. 21 (2012) 65–68.
[99] A. Darwiche, C. Marino, M.T. Sougrati, B. Fraisse, L. Stievano, L. Monconduit, J. Am. Chem. Soc. 134 (2012) 20805–20811.
[100] J. Qian, Y. Chen, L. Wu, Y. Cao, X. Ai, H. Yang, Chem. Commun. 48 (2012) 7070–7072.
[101] H. Lu, L. Wu, L. Xiao, X. Ai, H. Yang, Y. Cao, Electrochim. Acta 190 (2016) 402–408.
[102] Y. Kim, Y. Park, A. Choi, N.S. Choi, J. Kim, J. Lee, J.H. Ryu, S.M. Oh, K.T. Lee, Adv. Mater. 25 (2013) 3045–3049.
[103] J. Qian, X. Wu, Y. Cao, X. Ai, H. Yang, Angew. Chemie - Int. Ed. 52 (2013) 4633–4636.
[104] M. Dahbi, N. Yabuuchi, M. Fukunishi, K. Kubota, K. Chihara, K. Tokiwa, X.F. Yu, H. Ushiyama, K. Yamashita, J.Y. Son, Y.T. Cui, H. Oji, S. Komaba, Chem. Mater. 28 (2016) 1625–1635.
[105] Q. Li, Z. Zhang, S. Dong, C. Li, X. Ge, Z. Li, J. Ma, L. Yin, Part. Part. Syst. Charact. 34 (2017) 1600115.
[106] B. Farbod, K. Cui, W.P. Kalisvaart, M. Kupsta, B. Zahiri, A. Kohandehghan, E.M. Lotfabad, Z. Li, E.J. Luber, D. Mitlin, ACS Nano 8 (2014) 4415–4429.
[107] L. Baggetto, J.K. Keum, J.F. Browning, G.M. Veith, Electrochem. Commun. 34 (2013) 41–44.

[108] P. Xue, N. Wang, Z. Fang, Z. Lu, X. Xu, L. Wang, Y. Du, X. Ren, Z. Bai, S. Dou, G. Yu, Nano Lett. 19 (2019) 1998–2004.
[109] C. Wang, L. Wang, F. Li, F. Cheng, J. Chen, Adv. Mater. 29 (2017) 1–7.
[110] S. Liu, J. Feng, X. Bian, J. Liu, H. Xu, J. Mater. Chem. A 4 (2016) 10098–10104.
[111] Y. Han, N. Lin, T. Xu, T. Li, J. Tian, Y. Zhu, Y. Qian, Nanoscale 10 (2018) 3153–3158.
[112] M.K. Jangid, A. Vemulapally, F.J. Sonia, M. Aslam, A. Mukhopadhyay, J. Electrochem. Soc. 164 (2017) A2559–A2565.
[113] S. Huang, L. Liu, Y. Zheng, Y. Wang, D. Kong, Y. Zhang, Y. Shi, L. Zhang, O.G. Schmidt, H.Y. Yang, Adv. Mater. 30 (2018) 1–8.
[114] L. Zhang, X. Hu, C. Chen, H. Guo, X. Liu, G. Xu, H. Zhong, S. Cheng, P. Wu, J. Meng, Y. Huang, S. Dou, H. Liu, Adv. Mater. 29 (2017) 1604708.
[115] A. Darwiche, R. Dugas, B. Fraisse, L. Monconduit, J. Power Sources 304 (2016) 1–8.
[116] Y.R. Lim, F. Shojaei, K. Park, C.S. Jung, J. Park, W. Il Cho, H.S. Kang, Nanoscale 10 (2018) 7047–7057.
[117] S. Fang, D. Bresser, S. Passerini, Adv. Energy Mater. 10 (2020) 1902485.
[118] X. Yang, H.-J. Liang, H.-Y. Yu, M.-Y. Wang, X.-X. Zhao, X.-T. Wang, X.-L. Wu, J. Phys. Mater. 3 (2020) 042004.
[119] P. Zhou, M. Zhang, L. Wang, Q. Huang, Z. Su, L. Li, X. Wang, Y. Li, C. Zeng, Z. Guo, Front. Chem. 7 (2019) 1–10.
[120] Y. Zhong, X. Xia, F. Shi, J. Zhan, J. Tu, H.J. Fan, Adv. Sci. 3 (2016) 1500286.
[121] G. Chang, Y. Zhao, L. Dong, D.P. Wilkinson, L. Zhang, Q. Shao, W. Yan, X. Sun, J. Zhang, J. Mater. Chem. A 8 (2020) 4996–5048.
[122] M.N. Guzik, R. Mohtadi, S. Sartori, J. Mater. Res. 34 (2019) 877–904.
[123] F. Klein, B. Jache, A. Bhide, P. Adelhelm, Phys. Chem. Chem. Phys. 15 (2013) 15876–15887.
[124] Z. Song, H. Zhou, Energy Environ. Sci. 6 (2013) 2280–2301.
[125] X. Yin, S. Sarkar, S. Shi, Q.-A. Huang, H. Zhao, L. Yan, Y. Zhao, J. Zhang, Adv. Funct. Mater. 30 (2020) 1908445.
[126] Y. Park, D.S. Shin, S.H. Woo, N.S. Choi, K.H. Shin, S.M. Oh, K.T. Lee, S.Y. Hong, Adv. Mater. 24 (2012) 3562–3567.
[127] L. Zhao, J. Zhao, Y.S. Hu, H. Li, Z. Zhou, M. Armand, L. Chen, Adv. Energy Mater. 2 (2012) 962–965.
[128] V.-A. Oltean, S. Renault, M. Valvo, D. Brandell, Materials (Basel). 9 (2016) 142.
[129] M. López-Herraiz, E. Castillo-Martínez, J. Carretero-González, J. Carrasco, T. Rojo, M. Armand, Energy Environ. Sci. 8 (2015) 3233–3241.
[130] T. Sun, Z.J. Li, H.G. Wang, D. Bao, F.L. Meng, X.B. Zhang, Angew. Chemie - Int. Ed. 55 (2016) 10662–10666.
[131] R. Alcántara, J.M. Jiménez Mateos, J.L. Tirado, J. Electrochem. Soc. 149 (2002) A201.
[132] Y. Li, L. Mu, Y.S. Hu, H. Li, L. Chen, X. Huang, Energy Storage Mater. 2 (2016) 139–145.
[133] J. Jin, Z.Q. Shi, C.Y. Wang, Electrochim. Acta 141 (2014) 302–310.
[134] J. Zhu, J. Roscow, S. Chandrasekaran, L. Deng, P. Zhang, T. He, K. Wang, L. Huang, ChemSusChem 13 (2020) 1275–1295.
[135] P. Yu, W. Tang, F.F. Wu, C. Zhang, H.Y. Luo, H. Liu, Z.G. Wang, Rare Met. 39 (2020) 1019–1033.
[136] J. Górka, C. Vix-Guterl, C. Matei Ghimbeu, C 2 (2016) 24.
[137] D.A. Stevens, J.R. Dahn, J. Electrochem. Soc. 147 (2000) 1271.
[138] C. Bommier, T.W. Surta, M. Dolgos, X. Ji, Nano Lett. 15 (2015) 5888–5892.
[139] S. Alvin, D. Yoon, C. Chandra, H.S. Cahyadi, J.H. Park, W. Chang, K.Y. Chung, J. Kim, Carbon N. Y. 145 (2019) 67–81.
[140] N. Sun, Z. Guan, Y. Liu, Y. Cao, Q. Zhu, H. Liu, Z. Wang, P. Zhang, B. Xu, Adv. Energy Mater. 9 (2019) 1–14.
[141] B. Zhang, C.M. Ghimbeu, C. Laberty, C. Vix-Guterl, J.M. Tarascon, Adv. Energy Mater. 6 (2016) 1–9.
[142] D. Alvira, D. Antorán, J.J. Manyà, Chem. Eng. J. 447 (2022).
[143] S.L. Chou, Y. Pan, J.Z. Wang, H.K. Liu, S.X. Dou, Phys. Chem. Chem. Phys. 16 (2014) 20347–20359.
[144] C. Bommier, X. Ji, Small 14 (2018) 1–20.
[145] M. Dubois, J. Ghanbaja, D. Billaud, Synth. Met. 90 (1997) 127–134.
[146] W. Zhang, M. Dahbi, S. Komaba, Curr. Opin. Chem. Eng. 13 (2016) 36–44.
[147] L.O. Vogt, M. El Kazzi, E. Jämstorp Berg, S. Pérez Villar, P. Novák, C. Villevieille, Chem. Mater. 27 (2015) 1210–1216.
[148] J. Li, Y. Lu, T. Yang, D. Ge, D.L. Wood, Z. Li, IScience 23 (2020) 101081.
[149] L. Qiu, Z. Shao, D. Wang, F. Wang, W. Wang, J. Wang, Carbohydr. Polym. 112 (2014) 532–538.
[150] S.L. Chou, J.Z. Wang, H.K. Liu, S.X. Dou, J. Phys. Chem. C 115 (2011) 16220–16227.
[151] H. Buqa, M. Holzapfel, F. Krumeich, C. Veit, P. Novák, J. Power Sources 161 (2006) 617–622.
[152] A. Birrozzi, M. Copley, J. von Zamory, M. Pasqualini, S. Calcaterra, F. Nobili, A. Di Cicco, H. Rajantie, M. Briceno, E. Bilbé, L. Cabo-Fernandez, L.J. Hardwick, D. Bresser, S. Passerini, J. Electrochem. Soc. 162 (2015) A2331–A2338.
[153] N.P.W. Pieczonka, V. Borgel, B. Ziv, N. Leifer, V. Dargel, D. Aurbach, J.-H. Kim, Z. Liu, X. Huang, S.A. Krachkovskiy, G.R. Goward, I. Halalay, B.R. Powell, A. Manthiram, Adv. Energy Mater. 5 (2015) 1501008.
[154] F. De Giorgio, A. La Monaca, A. Dinter, M. Frankenberger, K.H. Pettinger, C. Arbizzani, Electrochim. Acta 289 (2018) 112–119.
[155] C. Chen, S.H. Lee, M. Cho, J. Kim, Y. Lee, ACS Appl. Mater. Interfaces 8 (2016) 2658–2665.
[156] D. Versaci, R. Nasi, U. Zubair, J. Amici, M. Sgroi, M.A. Dumitrescu, C. Francia, S. Bodoardo, N. Penazzi, J. Solid State Electrochem. 21 (2017) 3429–3435.
[157] M. Bele, M. Gaberscek, R. Dominko, J. Drofenik, K.Y. Zupan, P. Komac, K. Kocevar, I. Musevic, S. Pejovnik, Carbon N. Y. 40 (2002) 1117–1122.
[158] B. Tran, I.O. Oladeji, Z. Wang, J. Calderon, G. Chai, D. Atherton, L. Zhai, Electrochim. Acta 88 (2013) 536–542.
[159] Y. Ma, K. Chen, J. Ma, G. Xu, S. Dong, B. Chen, J. Li, Z. Chen, X. Zhou, G. Cui, Energy Environ. Sci. 12 (2019) 273–280.
[160] J. Domínguez-Robles, R. Sánchez, P. Díaz-Carrasco, E. Espinosa, M.T. García-Domínguez, A. Rodríguez, Int. J. Biol. Macromol. 104 (2017) 909–918.
[161] M. Dahbi, T. Nakano, N. Yabuuchi, T. Ishikawa, K. Kubota, M. Fukunishi, S. Shibahara, J.Y. Son, Y.T. Cui, H. Oji, S. Komaba, Electrochem. Commun. 44 (2014) 66–69.
[162] C. Clasen, W.-M. Kulicke, Prog. Polym. Sci. 26 (2001) 1839–1919.
[163] B.R. Lee, E.S. Oh, J. Phys. Chem. C 117 (2013) 4404–4409.
[164] Y. Morikawa, Y. Yamada, K. Doi, S.I. Nishimura, A. Yamada, Electrochemistry 88 (2020) 151–156.
[165] P. Bai, X. Han, Y. He, P. Xiong, Y. Zhao, J. Sun, Y. Xu, Energy Storage Mater. 25 (2020) 324–333.
[166] X. Song, T. Meng, Y. Deng, A. Gao, J. Nan, D. Shu, F. Yi, Electrochim. Acta 281 (2018) 370–377.
[167] C.C. Wu, C.C. Li, ACS Sustain. Chem. Eng. 8 (2020) 6868–6876.
[168] R. Zhang, X. Yang, D. Zhang, H. Qiu, Q. Fu, H. Na, Z. Guo, F. Du, G. Chen, Y. Wei, J. Power Sources 285 (2015) 227–234.
[169] R. Muruganantham, T.H. Hsieh, C.H. Lin, W.R. Liu, Mater. Today Energy 14 (2019) 100346.
[170] F. Linsenmann, D. Pritzl, H.A. Gasteiger, J. Electrochem. Soc. 166 (2019) A3668–A3674.
[171] F. Linsenmann, D. Pritzl, H.A. Gasteiger, J. Electrochem. Soc. 168 (2021) 010506.
[172] Q. Zhang, X. Deng, M. Ji, Y. Li, Z. Shi, Ionics (Kiel). 26 (2020) 4523–4532.
[173] J. Wang, L. Yan, Q. Ren, L. Fan, F. Zhang, Z. Shi, Electrochim. Acta 291 (2018) 188–196.
[174] P. Wang, L. Fan, L. Yan, Z. Shi, J. Alloys Compd. 775 (2019) 1028–1035.
[175] D. Li, Y. Zhu, E. Xu, H. Wang, T. Chen, J. Quan, Y. Zhang, L. Wang, Y. Jiang, New J. Chem. 43 (2019) 10449–10457.
[176] K. Nakabayashi, H. Yi, D.Y. Ryu, D. Chung, J. Miyawaki, S.H. Yoon, Chem. Lett. 48 (2019) 753–755.
[177] S. Ikram, S. Dsoke, A. Sarapulova, M. Müller, U.A. Rana, H.M. Siddiqi, J. Electrochem. Soc. 167 (2020) 100531.
[178] Y. Kim, J.K. Kim, C. Vaalma, G.H. Bae, G.T. Kim, S. Passerini, Y. Kim, Carbon N. Y. 129 (2018) 564–571.
[179] Y. Kim, Y. Kim, A. Choi, S. Woo, D. Mok, N.S. Choi, Y.S. Jung, J.H. Ryu, S.M. Oh, K.T. Lee, Adv. Mater. 26 (2014) 4139–4144.
[180] F. Zhao, N. Han, W. Huang, J. Li, H. Ye, F. Chen, Y. Li, J. Mater. Chem. A 3 (2015) 21754–21759.
[181] W.J. Li, S.L. Chou, J.Z. Wang, H.K. Liu, S.X. Dou, Chem. Commun. 51 (2015) 3682–3685.
[182] Z. Zhang, T. Zeng, Y. Lai, M. Jia, J. Li, J. Power Sources 247 (2014) 1–8.
[183] W. Zhang, M. Dahbi, S. Amagasa, Y. Yamada, S. Komaba, Electrochem. Commun. 69 (2016) 11–14.
[184] Q. Fan, W. Zhang, J. Duan, K. Hong, L. Xue, Y. Huang, Electrochim. Acta 174 (2015) 970–977.
[185] H. Darjazi, A. Staffolani, L. Sbrascini, L. Bottoni, R. Tossici, F. Nobili, Energies 13 (2020) 6216.
[186] E. De La Llave, V. Borgel, E. Zinigrad, F.F. Chesneau, P. Hartmann, Y.K. Sun, D. Aurbach, Isr. J. Chem. 55 (2015) 1260–1274.
[187] X. He, J. Liao, Z. Tang, L. Xiao, X. Ding, Q. Hu, Z. Wen, C. Chen, J. Power Sources 396 (2018) 533–541.
[188] Y. Qi, Y. Lu, L. Liu, X. Qi, F. Ding, H. Li, X. Huang, L. Chen, Y.S. Hu, Energy Storage Mater. 26 (2020) 577–584.
[189] X. Lin, Y. Liu, H. Tan, B. Zhang, Carbon N. Y. 157 (2020) 316–323.
[190] Y. Zheng, Y. Lu, X. Qi, Y. Wang, L. Mu, Y. Li, Q. Ma, J. Li, Y.S. Hu, Energy Storage Mater. 18 (2019) 269–279.
[191] M.K. Rybarczyk, Y. Li, M. Qiao, Y.S. Hu, M.M. Titirici, M. Lieder, J. Energy Chem. 29 (2019) 17–22.
[192] Y. Li, Y. Lu, Q. Meng, A.C.S. Jensen, Q. Zhang, Q. Zhang, Y. Tong, Y. Qi, L. Gu, M. Titirici, Y. Hu, Adv. Energy Mater. 9 (2019) 1902852.
[193] A. Beda, C. Villevieille, P. Taberna, P. Simon, C. Matei Ghimbeu, J. Mater. Chem. A 8 (2020) 5558–5571.
[194] H. Li, F. Shen, W. Luo, J. Dai, X. Han, Y. Chen, Y. Yao, H. Zhu, K. Fu, E. Hitz, L. Hu, ACS Appl. Mater. Interfaces 8 (2016) 2204–2210.
[195] F. Shen, W. Luo, J. Dai, Y. Yao, M. Zhu, E. Hitz, Y. Tang, Y. Chen, V.L. Sprenkle, X. Li, L. Hu, Adv. Energy Mater. 6 (2016) 1600377.
[196] T. Jin, Q. Han, L. Jiao, Adv. Mater. 32 (2020) 1–14.
[197] A.J. Bard, L.R. Faulkner, Electrochemical Methods Fundamentals and Applications, 2nd ed., John Wiley & Sons, New York, Chichester, Weinheim, Brisbane, Singapore, Toronto, 1981.
[198] J.L. Gómez-Cámer, P. Novák, Electrochem. Commun. 34 (2013) 208–210.
[199] F. La Mantia, C.D. Wessells, H.D. Deshazer, Y. Cui, Electrochem. Commun. 31 (2013) 141–144.
[200] D.P. Abraham, S.D. Poppen, A.N. Jansen, J. Liu, D.W. Dees, Electrochim. Acta 49 (2004) 4763–4775.
[201] M. Dollé, F. Orsini, A.S. Gozdz, J.-M. Tarascon, J. Electrochem. Soc. 148 (2001) A851.
[202] N. Mozhzhukhina, E.J. Calvo, J. Electrochem. Soc. 164 (2017) A2295–A2297.
[203] A.N. Jansen, D.W. Dees, D.P. Abraham, K. Amine, G.L. Henriksen, J. Power Sources 174 (2007) 373–379.
[204] D.W. Dees, A.N. Jansen, D.P. Abraham, J. Power Sources 174 (2007) 1001–1006.

[205] H. Nara, D. Mukoyama, T. Yokoshima, T. Momma, T. Osaka, J. Electrochem. Soc. 163 (2016) A434–A441.
[206] M.W. Verbrugge, D.R. Baker, B.J. Koch, J. Power Sources 110 (2002) 295–309.
[207] F.J. Simon, L. Blume, M. Hanauer, U. Sauter, J. Janek, J. Electrochem. Soc. 165 (2018) A1363–A1371.
[208] J. Costard, M. Ender, M. Weiss, E. Ivers-Tiffée, J. Electrochem. Soc. 164 (2017) A80–A87.
[209] D. Juarez-Robles, C.F. Chen, Y. Barsukov, P.P. Mukherjee, J. Electrochem. Soc. 164 (2017) A837–A847.
[210] R. Tatara, P. Karayaylali, Y. Yu, Y. Zhang, L. Giordano, F. Maglia, R. Jung, J.P. Schmidt, I. Lund, Y. Shao-Horn, J. Electrochem. Soc. 166 (2019) A5090–A5098.
[211] S. Yi, B. Wang, Z. Chen, R. Wang, D. Wang, RSC Adv. 8 (2018) 18597–18603.
[212] A. Ikezawa, G. Fukunishi, T. Okajima, F. Kitamura, K. Suzuki, M. Hirayama, R. Kanno, H. Arai, Electrochem. Commun. 116 (2020) 106743.
[213] M.D. Levi, V. Dargel, Y. Shilina, D. Aurbach, I.C. Halalay, Electrochim. Acta 149 (2014) 126–135.
[214] J. Hou, R. Girod, N. Nianias, T.-H. Shen, J. Fan, V. Tileli, J. Electrochem. Soc. 167 (2020) 110515.
[215] A. Gomez-Martin, J. Martinez-Fernandez, M. Ruttert, M. Winter, T. Placke, J. Ramirez-Rico, Chem. Mater. 31 (2019) 7288–7299.
[216] Z.V. Bobyleva, O.A. Drozhzhin, K.A. Dosaev, A. Kamiyama, S.V. Ryazantsev, S. Komaba, E.V. Antipov, Electrochim. Acta 354 (2020) 136647.
[217] L. Wu, D. Buchholz, C. Vaalma, G.A. Giffin, S. Passerini, ChemElectroChem 3 (2016) 292–298.
[218] M.J. Piernas-Muñoz, E. Castillo-Martínez, J.L. Gómez-Cámer, T. Rojo, Electrochim. Acta 200 (2016) 123–130.
[219] D.S. Tchitchekova, D. Monti, P. Johansson, F. Bardé, A. Randon-Vitanova, M.R. Palacín, A. Ponrouch, J. Electrochem. Soc. 164 (2017) A1384–A1392.
[220] S.E. Lee, M.H. Tang, Electrochem. Commun. 100 (2019) 70–73.
[221] M. Moshkovich, Y. Gofer, D. Aurbach, J. Electrochem. Soc. 148 (2001) E155.
[222] G.G. Eshetu, T. Diemant, M. Hekmatfar, S. Grugeon, R.J. Behm, S. Laruelle, M. Armand, S. Passerini, Nano Energy 55 (2019) 327–340.
[223] G.G. Eshetu, G.A. Elia, M. Armand, M. Forsyth, S. Komaba, T. Rojo, S. Passerini, Adv. Energy Mater. 10 (2020) 2000093.
[224] Y. Wang, Z. Feng, W. Zhu, V. Gariépy, C. Gagnon, M. Provencher, D. Laul, R. Veillette, M. Trudeau, A. Guerfi, K. Zaghib, Materials (Basel). 11 (2018) 1294.
[225] C. Geng, D. Buchholz, G.T. Kim, D.V. Carvalho, H. Zhang, L.G. Chagas, S. Passerini, Small Methods 3 (2019) 1–9.
[226] J. Fondard, E. Irisarri, C. Courrèges, M.R. Palacin, A. Ponrouch, R. Dedryvère, J. Electrochem. Soc. 167 (2020) 070526.
[227] M. Lu, Y. Huang, C. Chen, Energy and Fuels 34 (2020) 11489–11497.
[228] G.G. Eshetu, S. Grugeon, H. Kim, S. Jeong, L. Wu, G. Gachot, S. Laruelle, M. Armand, S. Passerini, ChemSusChem 9 (2016) 462–471.
[229] H. Kumar, E. Detsi, D.P. Abraham, V.B. Shenoy, Chem. Mater. 28 (2016) 8930–8941.
[230] M. Dahbi, T. Nakano, N. Yabuuchi, S. Fujimura, K. Chihara, K. Kubota, J.Y. Son, Y.T. Cui, H. Oji, S. Komaba, ChemElectroChem 3 (2016) 1856–1867.
[231] Y. Pan, Y. Zhang, B.S. Parimalam, C.C. Nguyen, G. Wang, B.L. Lucht, J. Electroanal. Chem. 799 (2017) 181–186.
[232] H. Lee, Y. Il Kim, J.K. Park, J.W. Choi, Chem. Commun. 48 (2012) 8416–8418.
[233] J. Zhao, L. Zhao, K. Chihara, S. Okada, J.I. Yamaki, S. Matsumoto, S. Kuze, K. Nakane, J. Power Sources 244 (2013) 752–757.
[234] J.Y. Jang, H. Kim, Y. Lee, K.T. Lee, K. Kang, N.S. Choi, Electrochem. Commun. 44 (2014) 74–77.
[235] C. Chen, M. Wu, J. Liu, Z. Xu, K. Zaghib, Y. Wang, J. Power Sources 471 (2020) 228455.
[236] L. Ji, M. Gu, Y. Shao, X. Li, M.H. Engelhard, B.W. Arey, W. Wang, Z. Nie, J. Xiao, C. Wang, J.G. Zhang, J. Liu, Adv. Mater. 26 (2014) 2901–2908.
[237] A. Bouibes, N. Takenaka, T. Fujie, K. Kubota, S. Komaba, M. Nagaoka, A.C.S. Appl, Mater. Interfaces 10 (2018) 28525–28532.
[238] D.H. Kim, B. Kang, H. Lee, J. Power Sources 423 (2019) 137–143.
[239] H. Che, X. Yang, H. Wang, X.Z. Liao, S.S. Zhang, C. Wang, Z.F. Ma, J. Power Sources 407 (2018) 173–179.
[240] M. Goktas, C. Bolli, E.J. Berg, P. Novák, K. Pollok, F. Langenhorst, M.V. Roeder, O. Lenchuk, D. Mollenhauer, P. Adelhelm, Adv. Energy Mater. 8 (2018) 1–11.
[241] B. Jache, P. Adelhelm, Angew. Chemie 126 (2014) 10333–10337.
[242] Z. Zhu, F. Cheng, Z. Hu, Z. Niu, J. Chen, J. Power Sources 293 (2015) 626–634.
[243] I. Hasa, X. Dou, D. Buchholz, Y. Shao-Horn, J. Hassoun, S. Passerini, B. Scrosati, J. Power Sources 310 (2016) 26–31.
[244] H. Kim, J. Hong, Y.U. Park, J. Kim, I. Hwang, K. Kang, Adv. Funct. Mater. 25 (2015) 534–541.
[245] Y.E. Zhu, L. Yang, X. Zhou, F. Li, J. Wei, Z. Zhou, J. Mater. Chem. A 5 (2017) 9528–9532.
[246] Y. He, P. Bai, S. Gao, Y. Xu, ACS Appl. Mater. Interfaces 10 (2018) 41380–41388.
[247] B. Xiao, F.A. Soto, M. Gu, K.S. Han, J. Song, H. Wang, M.H. Engelhard, V. Murugesan, K.T. Mueller, D. Reed, V.L. Sprenkle, P.B. Balbuena, X. Li, Adv. Energy Mater. 8 (2018) 1–10.
[248] K. Li, J. Zhang, D. Lin, D.W. Wang, B. Li, W. Lv, S. Sun, Y.B. He, F. Kang, Q.H. Yang, L. Zhou, T.Y. Zhang, Nat. Commun. 10 (2019) 1–10.
[249] J. Zhang, D.W. Wang, W. Lv, S. Zhang, Q. Liang, D. Zheng, F. Kang, Q.H. Yang, Energy Environ. Sci. 10 (2017) 370–376.
[250] A. Mahmood, S. Li, Z. Ali, H. Tabassum, B. Zhu, Z. Liang, W. Meng, W. Aftab, W. Guo, H. Zhang, M. Yousaf, S. Gao, R. Zou, Y. Zhao, Adv. Mater. 31 (2019) 1–10.
[251] P. Bai, Y. He, P. Xiong, X. Zhao, K. Xu, Y. Xu, Energy Storage Mater. 13 (2018) 274–282.
[252] D.R. MacFarlane, M. Forsyth, P.C. Howlett, M. Kar, S. Passerini, J.M. Pringle, H. Ohno, M. Watanabe, F. Yan, W. Zheng, S. Zhang, J. Zhang, Nat. Rev. Mater. 1 (2016) 15005.
[253] W. Zhou, M. Zhang, X. Kong, W. Huang, Q. Zhang, Adv. Sci. 8 (2021) 2004490.
[254] C.H. Wang, Y.W. Yeh, N. Wongittharom, Y.C. Wang, C.J. Tseng, S.W. Lee, W.S. Chang, J.K. Chang, J. Power Sources 274 (2015) 1016–1023.
[255] F. Makhlooghiazad, R. Yunis, D. Mecerreyes, M. Armand, P.C. Howlett, M. Forsyth, Solid State Ionics 312 (2017) 44–52.
[256] F. Wu, N. Zhu, Y. Bai, L. Liu, H. Zhou, C. Wu, ACS Appl. Mater. Interfaces 8 (2016) 21381–21386.
[257] M. Forsyth, H. Yoon, F. Chen, H. Zhu, D.R. MacFarlane, M. Armand, P.C. Howlett, J. Phys. Chem. C 120 (2016) 4276–4286.
[258] T. Carstens, A. Lahiri, N. Borisenko, F. Endres, J. Phys. Chem. C 120 (2016) 14736–14741.
[259] H. Sun, G. Zhu, X. Xu, M. Liao, Y.Y. Li, M. Angell, M. Gu, Y. Zhu, W.H. Hung, J. Li, Y. Kuang, Y. Meng, M.C. Lin, H. Peng, H. Dai, Nat. Commun. 10 (2019) 1–11.
[260] M. Bellusci, E. Simonetti, M. De Francesco, G.B. Appetecchi, Appl. Sci. 10 (2020) 6323.
[261] D. Monti, E. Jónsson, M.R. Palacín, P. Johansson, J. Power Sources 245 (2014) 630–636.
[262] X. Wang, Z. Shang, A. Yang, Q. Zhang, F. Cheng, D. Jia, J. Chen, Chem 5 (2019) 364–375.
[263] M. Liu, H. Ao, Y. Jin, Z. Hou, X. Zhang, Y. Zhu, Y. Qian, Mater. Today Energy 17 (2020) 100432.
[264] D. Bin, F. Wang, A.G. Tamirat, L. Suo, Y. Wang, C. Wang, Y. Xia, Adv. Energy Mater. 8 (2018) 1703008.
[265] Y. Wang, X. Meng, J. Sun, Y. Liu, L. Hou, Front. Chem. 8 (2020) 1–8.
[266] F. Malchik, N. Shpigel, M.D. Levi, T.R. Penki, B. Gavriel, G. Bergman, M. Turgeman, D. Aurbach, Y. Gogotsi, Nano Energy 79 (2021) 105433.
[267] K. Nakamoto, R. Sakamoto, M. Ito, A. Kitajou, S. Okada, Electrochemistry 85 (2017) 179–185.
[268] R. Chandrasekaran, S. Selladurai, J. Solid State Electrochem. 5 (2001) 355–361.
[269] Q. Zhang, Y. Lu, H. Yu, G. Yang, Q. Liu, Z. Wang, L. Chen, Y.-S. Hu, J. Electrochem. Soc. 167 (2020) 070523.
[270] A. Boschin, P. Johansson, Electrochim. Acta 175 (2015) 124–133.
[271] J.S. Moreno, M. Armand, M.B. Berman, S.G. Greenbaum, B. Scrosati, S. Panero, J. Power Sources 248 (2014) 695–702.
[272] Y.L. Ni'Mah, M.Y. Cheng, J.H. Cheng, J. Rick, B.J. Hwang, J. Power Sources 278 (2015) 375–381.
[273] L. Liu, X. Qi, S. Yin, Q. Zhang, X. Liu, L. Suo, H. Li, L. Chen, Y.S. Hu, ACS Energy Lett. 4 (2019) 1650–1657.
[274] L. Qiao, X. Judez, T. Rojo, M. Armand, H. Zhang, J. Electrochem. Soc. 167 (2020) 070534.
[275] F. Colò, F. Bella, J.R. Nair, C. Gerbaldi, J. Power Sources 365 (2017) 293–302.
[276] D.T. Vo, H.N. Do, T.T. Nguyen, T.T.H. Nguyen, V.M. Tran, S. Okada, M.L.P. Le, Mater. Sci. Eng. B Solid-State Mater. Adv. Technol. 241 (2019) 27–35.
[277] K. Vignarooban, P. Badami, M.A.K.L. Dissanayake, P. Ravirajan, A.M. Kannan, Ionics (Kiel). 23 (2017) 2817–2822.
[278] W. Zhao, J. Yi, P. He, H. Zhou, Solid-State Electrolytes for Lithium-Ion Batteries: Fundamentals, Challenges and Perspectives, Springer, Singapore, 2019.
[279] J.-J. Kim, K. Yoon, I. Park, K. Kang, Small Methods 1 (2017) 1700219.
[280] Y. Wang, S. Song, C. Xu, N. Hu, J. Molenda, L. Lu, Nano Mater. Sci. 1 (2019) 91–100.
[281] E. Talaie, P. Bonnick, X. Sun, Q. Pang, X. Liang, L.F. Nazar, Chem. Mater. 29 (2017) 90–105.
[282] T. Marks, S. Trussler, A.J. Smith, D. Xiong, J.R. Dahn, J. Electrochem. Soc. 158 (2011) 51–57.
[283] P. Bonnick, J.R. Dahn, J. Electrochem. Soc. 159 (2012) A981–A989.
[284] M. Chamas, M.T. Sougrati, C. Reibel, P.E. Lippens, Chem. Mater. 25 (2013) 2410–2420.
[285] G.G. Amatucci, F. Badway, A. Du Pasquier, T. Zheng, J. Electrochem. Soc. 148 (2001) A930.
[286] S. Klink, E. Madej, E. Ventosa, A. Lindner, W. Schuhmann, F. La Mantia, Electrochem. Commun. 22 (2012) 120–123.
[287] M. Ender, A. Weber, I.-T. Ellen, J. Electrochem. Soc. 159 (2011) A128–A136.
[288] S. Rubio, R.R. Maça, M.J. Aragón, M. Cabello, M. Castillo-Rodríguez, P. Lavela, J. L. Tirado, V. Etacheri, G.F. Ortiz, J. Power Sources 432 (2019) 82–91.
[289] J.W. Choi, D. Aurbach, Nat. Rev. Mater. 1 (2016) 16013.
[290] G. Yan, R. Dugas, J.-M. Tarascon, J. Electrochem. Soc. 165 (2018) A220–A227.
[291] M. Morcrette, Y. Chabre, G. Vaughan, G. Amatucci, J.B. Leriche, S. Patoux, C. Masquelier, J.M. Tarascon, Electrochim. Acta 47 (2002) 3137–3149.
[292] C. Villevieille, T. Sasaki, P. Novák, RSC Adv. 4 (2014) 6782–6789.
[293] Q. Jacquet, A. Iadecola, M. Saubanère, L. Lemarquis, E.J. Berg, D. Alves Dalla Corte, G. Rousse, M.L. Doublet, J.M. Tarascon, Chem. Mater. 30 (2018) 7682–7690.
[294] A. Vizintin, J. Bitenc, A. Kopač Lautar, K. Pirnat, J. Grdadolnik, J. Stare, A. Randon-Vitanova, R. Dominko, Nat. Commun. 9 (2018) 661.
[295] N. Tsiouvaras, S. Meini, I. Buchberger, H.A. Gasteiger, J. Electrochem. Soc. 160 (2013) A471–A477.
[296] O. Pecher, J. Carretero-Gonzalez, K.J. Griffith, C.P. Grey, Chem. Mater. 29 (2017) 213–242.
[297] M. Wünsch, R. Füßler, D.U. Sauer, J. Energy Storage 20 (2018) 196–203.
[298] X. Xiang, K. Zhang, J. Chen, Adv. Mater. 27 (2015) 5343–5364.

[299] Z. Xu, F. Xie, J. Wang, H. Au, M. Tebyetekerwa, Z. Guo, S. Yang, Y. Hu, M. Titirici, Adv. Funct. Mater. 29 (2019) 1903895.
[300] C.A. Vincent, B. Scrosati, Modern Batteries, 2nd ed., Butterworth Heinemann, 1997.
[301] X. Yang, A.L. Rogach, Adv. Energy Mater. 9 (2019) 1–10.
[302] N. Elgrishi, K.J. Rountree, B.D. McCarthy, E.S. Rountree, T.T. Eisenhart, J.L. Dempsey, J. Chem. Educ. 95 (2018) 197–206.
[303] T. Zhang, J. Mao, X. Liu, M. Xuan, K. Bi, X.L. Zhang, J. Hu, J. Fan, S. Chen, G. Shao, RSC Adv. 7 (2017) 41504–41511.
[304] Q. Wang, X. Zhu, Y. Liu, Y. Fang, X. Zhou, J. Bao, Carbon N. Y. 127 (2018) 658–666.
[305] P.C. Rath, J. Patra, H.T. Huang, D. Bresser, T.Y. Wu, J.K. Chang, ChemSusChem 12 (2019) 2302–2309.
[306] M. Wahid, Y. Gawli, D. Puthusseri, A. Kumar, M.V. Shelke, S. Ogale, ACS Omega 2 (2017) 3601–3609.
[307] J. Wang, J. Polleux, J. Lim, B. Dunn, J. Phys. Chem. C 111 (2007) 14925–14931.
[308] H. Lindström, S. Södergren, A. Solbrand, H. Rensmo, J. Hjelm, A. Hagfeldt, S.E. Lindquist, J. Phys. Chem. B 101 (1997) 7710–7716.
[309] T. Brezesinski, J. Wang, S.H. Tolbert, B. Dunn, Nat. Mater. 9 (2010) 146–151.
[310] P. Wang, X. Zhu, Q. Wang, X. Xu, X. Zhou, J. Bao, J. Mater. Chem. A 5 (2017) 5761–5769.
[311] S. Alvin, D. Yoon, C. Chandra, R.F. Susanti, W. Chang, C. Ryu, J. Kim, J. Power Sources 430 (2019) 157–168.
[312] L.F. Zhao, Z. Hu, W.H. Lai, Y. Tao, J. Peng, Z.C. Miao, Y.X. Wang, S.L. Chou, H.K. Liu, S.X. Dou, Adv. Energy Mater. 11 (2021) 1–28.
[313] W. Weppner, R.A. Huggins, J. Electrochem. Soc. 124 (1977) 1569–1578.
[314] D.W. Dees, S. Kawauchi, D.P. Abraham, J. Prakash, J. Power Sources 189 (2009) 263–268.
[315] Y. Li, Y.S. Hu, M.M. Titirici, L. Chen, X. Huang, Adv. Energy Mater. 6 (2016) 1–9.
[316] X.H. Rui, N. Yesibolati, S.R. Li, C.C. Yuan, C.H. Chen, Solid State Ionics 187 (2011) 58–63.
[317] Y. Zhang, X. Li, P. Dong, G. Wu, J. Xiao, X. Zeng, Y. Zhang, X. Sun, ACS Appl. Mater. Interfaces 10 (2018) 42796–42803.
[318] P. Wang, K. Zhu, K. Ye, Z. Gong, R. Liu, K. Cheng, G. Wang, J. Yan, D. Cao, J. Colloid Interface Sci. 561 (2020) 203–210.
[319] Y.E. Zhu, H. Gu, Y.N. Chen, D. Yang, J. Wei, Z. Zhou, Ionics (Kiel). 24 (2018) 1075–1081.
[320] N. Sun, H. Liu, B. Xu, J. Mater. Chem. A 3 (2015) 20560–20566.
[321] S. Wang, F. Gong, S. Yang, J. Liao, M. Wu, Z. Xu, C. Chen, X. Yang, F. Zhao, B. Wang, Y. Wang, X. Sun, Adv. Funct. Mater. 28 (2018) 1–10.
[322] D. Qin, S. Chen, J. Solid State Electrochem. 21 (2017) 1305–1312.
[323] K. Tang, L. Fu, R.J. White, L. Yu, M.-M. Titirici, M. Antonietti, J. Maier, Adv. Energy Mater. 2 (2012) 873–877.
[324] Q. Li, J. Huang, L. Cao, J. He, Y. Wang, W. Wu, Y. He, J. Li, J. Electroanal. Chem. 854 (2019) 113554.
[325] K. Yu, X. Wang, H. Yang, Y. Bai, C. Wu, J. Energy Chem. 55 (2021) 499–508.
[326] Y. Shen, S. Sun, M. Yang, X. Zhao, J. Alloys Compd. 784 (2019) 1290–1296.
[327] H. Tang, M. Wang, T. Lu, L. Pan, Ceram. Int. 43 (2017) 4475–4482.
[328] S.J.R. Prabakar, J. Jeong, M. Pyo, Electrochim. Acta 161 (2015) 23–31.
[329] L. Xiao, H. Lu, Y. Fang, M.L. Sushko, Y. Cao, X. Ai, H. Yang, J. Liu, Adv. Energy Mater. 8 (2018) 1–7.
[330] C. Wang, J. Huang, H. Qi, L. Cao, Z. Xu, Y. Cheng, X. Zhao, J. Li, J. Power Sources 358 (2017) 85–92.
[331] E.M. Lotfabad, J. Ding, K. Cui, A. Kohandehghan, W.P. Kalisvaart, M. Hazelton, D. Mitlin, ACS Nano 8 (2014) 7115–7129.
[332] M. Lu, W. Yu, J. Shi, W. Liu, S. Chen, X. Wang, H. Wang, Electrochim. Acta 251 (2017) 396–406.
[333] W. Li, J. Huang, L. Feng, L. Cao, Y. Ren, R. Li, Z. Xu, J. Li, C. Yao, J. Alloys Compd. 716 (2017) 210–219.
[334] C. Bommier, D. Leonard, Z. Jian, W.F. Stickle, P.A. Greaney, X. Ji, Adv. Mater. Interfaces 3 (2016) 1–10.
[335] Z. Zhu, F. Liang, Z. Zhou, X. Zeng, D. Wang, P. Dong, J. Zhao, S. Sun, Y. Zhang, X. Li, J. Mater. Chem. A 6 (2018) 1513–1522.
[336] M. Liu, J. Zhang, S. Guo, B. Wang, Y. Shen, X. Ai, H. Yang, J. Qian, ACS Appl. Mater. Interfaces 12 (2020) 17620–17627.
[337] R. Li, J. Huang, W. Li, J. Li, L. Cao, Z. Xu, Y. He, A. Yu, G. Lu, Electrochim. Acta 313 (2019) 109–115.
[338] A. Raj K, M.R. Panda, D.P. Dutta, S. Mitra, Carbon N. Y. 143 (2019) 402–412.
[339] L. Yang, M. Hu, H. Zhang, W. Yang, R. Lv, J. Colloid Interface Sci. 566 (2020) 257–264.
[340] F. Wu, M. Zhang, Y. Bai, X. Wang, R. Dong, C. Wu, ACS Appl. Mater. Interfaces 11 (2019) 12554–12561.
[341] H. Göhr, in: Electrochem. Appl., ZAHNER-elektrik GmbH & Co. KG, 1997, pp. 2–3.
[342] D.W. Abarbanel, K.J. Nelson, J.R. Dahn, J. Electrochem. Soc. 163 (2016) A522–A529.
[343] J. Landesfeind, J. Hattendorff, A. Ehrl, W.A. Wall, H.A. Gasteiger, J. Electrochem. Soc. 163 (2016) A1373–A1387.
[344] N. Ogihara, Y. Itou, T. Sasaki, Y. Takeuchi, J. Phys. Chem. C 119 (2015) 4612–4619.
[345] N. Ogihara, S. Kawauchi, C. Okuda, Y. Itou, Y. Takeuchi, Y. Ukyo, J. Electrochem. Soc. 159 (2012) A1034–A1039.
[346] J. Illig, M. Ender, A. Weber, E. Ivers-Tiffée, J. Power Sources 282 (2015) 335–347.
[347] J. Landesfeind, D. Pritzl, H.A. Gasteiger, J. Electrochem. Soc. 164 (2017) A1773–A1783.
[348] D. Pritzl, J. Landesfeind, S. Solchenbach, H.A. Gasteiger, J. Electrochem. Soc. 165 (2018) A2145–A2153.
[349] M.E. Orazem, B. Tribollet, Electrochemical Impedance Spectroscopy, John Wiley & Sons Inc, 2008.
[350] Z. Li, Z. Jian, X. Wang, I.A. Rodríguez-Pérez, C. Bommier, X. Ji, Chem. Commun. 53 (2017) 2610–2613.
[351] A. Rudola, D. Aurbach, P. Balaya, Electrochem. Commun. 46 (2014) 56–59.
[352] Y. Zheng, Y. Wang, Y. Lu, Y.S. Hu, J. Li, Nano Energy 39 (2017) 489–498.
[353] C. Bünzli, H. Kaiser, P. Novák, J. Electrochem. Soc. 162 (2015) A218–A222.
[354] C.H. Chen, J. Liu, K. Amine, J. Power Sources 96 (2001) 321–328.
[355] R. Petibon, C.P. Aiken, N.N. Sinha, J.C. Burns, H. Ye, C.M. VanElzen, G. Jain, S. Trussler, J.R. Dahn, J. Electrochem. Soc. 160 (2013) A117–A124.
[356] T. Waldmann, M. Kasper, M. Wohlfahrt-Mehrens, Electrochim. Acta 178 (2015) 525–532.
[357] B.S. Haran, A. Durairajan, P. Ramadass, R.E. White, B.N. Popov, Proc. Intersoc. Energy Convers. Eng. Conf. 2 (2001) 935–940.
[358] R. Jung, R. Morasch, P. Karayaylali, K. Phillips, F. Maglia, C. Stinner, Y. Shao-Horn, H.A. Gasteiger, J. Electrochem. Soc. 165 (2018) A132–A141.
[359] M. Ender, J. Illig, E. Ivers-Tiffée, J. Electrochem. Soc. 164 (2017) A71–A79.
[360] S. Klink, D. Höche, F. La Mantia, W. Schuhmann, J. Power Sources 240 (2013) 273–280.
[361] R. Raccichini, M. Amores, G. Hinds, Batteries 5 (2019) 1–24.
[362] C. Delacourt, P.L. Ridgway, V. Srinivasan, V. Battaglia, J. Electrochem. Soc. 161 (2014) A1253–A1260.
[363] J. Newman, W. Tiedemann, J. Electrochem. Soc. 140 (2019) 1961–1968.
[364] H.M. Cho, Y.J. Park, J.W. Yeon, H.C. Shin, Electron. Mater. Lett. 5 (2009) 169–178.
[365] J. Zhou, P.H.L. Notten, J. Electrochem. Soc. 151 (2004) A2173.
[366] R. Morasch, B. Suthar, H.A. Gasteiger, J. Electrochem. Soc. 167 (2020) 100540.
[367] A.K. Kercher, D.C. Nagle, Carbon N. Y. 41 (2003) 15–27.
[368] K. Kim, D.G. Lim, C.W. Han, S. Osswald, V. Ortalan, J.P. Youngblood, V.G. Pol, A. C.S. Sustain, Chem. Eng. 5 (2017) 8720–8728.
[369] Y. Katsuyama, Y. Nakayasu, H. Kobayashi, Y. Goto, I. Honma, M. Watanabe, ChemSusChem 13 (2020) 5762–5768.
[370] C. Nita, B. Zhang, J. Dentzer, C. Matei Ghimbeu, J. Energy Chem. 58 (2021) 207–218.
[371] N. Sharma, W.K. Pang, Z. Guo, V.K. Peterson, ChemSusChem 8 (2015) 2826–2853.
[372] A.C. Ferrari, J. Robertson, Phys. Rev. B 61 (2000) 14095–14107.
[373] M.A. Pimenta, G. Dresselhaus, M.S. Dresselhaus, L.G. Cançado, A. Jorio, R. Saito, Phys. Chem. Chem. Phys. 9 (2007) 1276–1291.
[374] A. Beda, P.L. Taberna, P. Simon, C. Matei Ghimbeu, Carbon N. Y. 139 (2018) 248–257.
[375] G. Chollon, J. Takahashi, Compos. Part A Appl. Sci. Manuf. 30 (1999) 507–513.
[376] A. Sadezky, H. Muckenhuber, H. Grothe, R. Niessner, U. Pöschl, Carbon N. Y. 43 (2005) 1731–1742.
[377] L.G. Cançado, K. Takai, T. Enoki, M. Endo, Y.A. Kim, H. Mizusaki, A. Jorio, L.N. Coelho, R. Magalhães-Paniago, M.A. Pimenta, Appl. Phys. Lett. 88 (2006) 2–5.
[378] P. Bai, Y. He, X. Zou, X. Zhao, P. Xiong, Y. Xu, Adv. Energy Mater. 8 (2018) 1–9.
[379] J.S. Weaving, A. Lim, J. Millichamp, T.P. Neville, D. Ledwoch, E. Kendrick, P.F. McMillan, P.R. Shearing, C.A. Howard, D.J.L. Brett, ACS Appl. Energy Mater. 3 (2020) 7474–7484.
[380] J. Landers, G.Y. Gor, A.V. Neimark, Colloids Surfaces A Physicochem. Eng. Asp. 437 (2013) 3–32.
[381] M. Thommes, K.A. Cychosz, Adsorption 20 (2014) 233–250.
[382] Y. Matsukawa, F. Linsenmann, M.A. Plass, G. Hasegawa, K. Hayashi, T. Fellinger, Beilstein J. Nanotechnol. 11 (2020) 1217–1229.
[383] K.C. Kim, T.U. Yoon, Y.S. Bae, Microporous Mesoporous Mater. 224 (2016) 294–301.
[384] L. Froboese, P. Titscher, B. Westphal, W. Haselrieder, A. Kwade, Mater. Charact. 133 (2017) 102–111.
[385] Y. Li, Y.S. Hu, H. Li, L. Chen, X. Huang, J. Mater. Chem. A 4 (2015) 96–104.
[386] W. Tian, L. Wang, K. Huo, X. He, J. Power Sources 430 (2019) 60–66.
[387] P. Li, L. Yu, S. Ji, X. Xu, Z. Liu, J. Liu, J. Liu, Chem. Eng. J. 374 (2019) 502–510.
[388] C. Chen, Y. Huang, Z. Meng, Z. Xu, P. Liu, T. Li, J. Energy Chem. 54 (2021) 482–492.
[389] V. Simone, A. Boulineau, A. de Geyer, D. Rouchon, L. Simonin, S. Martinet, J. Energy Chem. 25 (2016) 761–768.
[390] I. Izanzar, M. Dahbi, M. Kiso, S. Doubaji, S. Komaba, I. Saadoune, Carbon N. Y. 137 (2018) 165–173.
[391] J.K. Mathiesen, R. Väli, M. Härmas, E. Lust, J. Fold Von Bülow, K.M.Ø. Jensen, P. Norby, J. Mater. Chem. A 7 (2019) 11709–11717.
[392] J.M. Stratford, P.K. Allan, O. Pecher, P.A. Chater, C.P. Grey, Chem. Commun. 52 (2016) 12430–12433.